Single droplets to particles - size, shape, shell thickness and porosity analyses using X-ray computed tomography

DOI:
10.1016/j.ces.2021.116879

Document Version
Accepted author manuscript

Single droplets to particles - size, shape, shell thickness and porosity analyses using X-ray computed tomography

Hassan Abdullahi[a], Petros Neoptolemou[a], Christopher L Burcham[b], Thomas Vetter[a,*]

[a]*University of Manchester, Department of Chemical Engineering and Analytical Science, M13 9PL Manchester, United Kingdom*

[b]*Eli Lilly and Company, Indianapolis, USA*

Abstract

The drying kinetics of single droplets of crystallizing and skin-forming species were investigated via acoustic levitation to provide a well-controlled environment mimicking spray drying operations. Particles manufactured by drying aqueous solution droplets containing varying ratios of D-mannitol and polyvinylpyrrolidone (PVP) were analysed using a range of techniques to elucidate their morphology and microstructure. Size, porosity and surface roughness of the manufactured particles increased with D-mannitol concentration in water, while the sphericity decreased, a consequence of the unique morphologies. The change in particle shell thickness was found to be minimal. Considering varying proportions of PVP led to a variety of fascinating structures, contrasting to those manufactured from pure D-mannitol. Temperature effects were further considered, and the results were matched by that from a lab and pilot scale spray dryer. Analysis of the solid form further demonstrates the opportunity to prepare different polymorphic forms of D-mannitol.

Keywords: Droplet drying, particle morphologies, particle microstructure, shape, porosity, shell thickness, X-ray computed tomography

*Corresponding author: phone +45 30 83 21 15.
Email address: vettert85@gmail.com (Thomas Vetter)

1. Introduction

The dispersibility, flowability and tabletability of powders is an important consideration in the manufacturing of pharmaceutical products [1]. These properties can be successfully tuned by crystallising particles of a desired morphology [2–4], or, more flexibly, by engineering the microstructure of the particles in a spray drying process [5–10]. Microstructure properties such as particle size, porosity and morphology can be tuned by altering the formulation and process conditions to affect powder processability and drug delivery efficiency. For example, it is possible to improve powder dispersibility for pulmonary drug delivery by engineering particles with a high degree of surface roughness (to reduce the cohesive forces between particles), or by tuning the size and apparent density of the particles [11, 12]. Since many active pharmaceutical ingredients (APIs) can exist in different solid forms i.e., amorphous structures and various crystalline forms, the microstructure and morphology of each phase presents different properties fundamental to particle and powder formulation [9, 12]. Amorphous particles are of particular interest in the pharmaceutical industry as they offer faster rates of dissolution and higher solubilities. This results in improved bioavailability of poorly soluble drugs [13, 14]. However, such forms usually need to be stabilised with the addition of an excipient (e.g., polymers) against transformation into more thermodynamically stable forms. Spray drying is a robust method that has been used extensively for powder manufacturing. The typically rapid kinetics and opportunity to co-formulate active ingredients with excipients allows generation of suitable stable amorphous particles, even for materials that have a strong tendency to crystallise. This single processing operation involving spray atomisation, droplet evaporation and particle formation therefore offers a unique opportunity to design tailor made particles [15].

Carrying out an in-depth investigation of particle morphology and microstructure directly on the scale of a typical spray dryer (that contains millions of droplets at any time) is difficult. Instead, single droplet studies are often used to understand how drying conditions affect the microstructure of the resulting dry particles [16–19]. Such an understanding requires powerful in situ and ex situ characterisation techniques, and often multiple methods to characterise various structural features of particulate materials (i.e., size, shape and porosity etc.). In the past, characterisation techniques such as confocal microscopy (to obtain information on sample heterogeneity), Raman spectroscopy and X-ray diffraction (to under-

stand the crystalline nature of samples) and optical imaging and scanning electron microscopy (to obtain information on size, shape and surface topology of samples) have been used [16, 20–23]). These techniques are excellent for extracting two dimensional (2D) information. However, their applicability is limited when three dimensional (3D) information of a body is desired, or when only a small sample size is available for characterisation [24]. To obtain microstructural information of the architecture of particles, X-ray computed tomography (XCT) is a powerful alternative. This imaging technique provides a non-destructive way to visualise the internal structure of the particles by reproducing the 3D volume of the object. The rendered 3D volume is produced through the reconstruction of the cross sectional XCT images of the object [25]. XCT has been used previously in the characterisation of size and shape [17, 26–29], porosity [17, 23, 26, 30] and the microstructure of solids [28, 31–33]. Since the robustness of imaging techniques such as XCT may be affected by the method of data collection, image reconstruction and image processing strategy employed, the method of analysis must be designed to optimise the representation of key information specific to the sample of interest [25, 34]. A detailed analysis will therefore employ a data variability analysis during data collection and processing [24].

The generation of individual particles using single droplet drying (SDD) techniques can be achieved in various ways. A complete review of the different SDD techniques (sessile droplet drying, acoustic levitation, filament method, falling droplet drying methods) commonly used is given by Fu et al. [35]. Although single droplet drying methods are not without drawbacks, key information on the morphological development of particles can be readily obtained and the particles are often comparable to the ones obtained from a spray dryer. For example, in the work by Nuzzo et al. [36] lactose particles produced via acoustic levitation and a lab-scale spray dryer were compared. The morphologies produced on both scales were similar. However, the authors noticed a difference in the surface composition of the manufactured particles, owing to the different time scales of the processes. The drying times resulting in single droplet drying experiments are often larger since SDD methods employ larger droplet sizes, typically 100 – 1500 µm compared to 10 – 100 µm in a typical spray drying operation, and smaller gas velocities. In a spray dryer, this difference typically leads to the generation of particles with smaller sizes, and a difference in the microstructure of particles as explained above [36–38]. Both et al. [16] investigated the morphology of particles obtained when milk is dried. Smooth particles with large indents were obtained in both sessile droplet drying method and by acoustic levitation, although two indents

were formed when using acoustic levitation, only one indent was observed using the sessile method as one end of the droplet is attached to a hydrophobic surface. Several other authors have investigated the drying kinetics, particle morphologies and other intrinsic properties such as stickiness and surface composition [20, 21, 29, 36, 39–42]. The study of single droplets allows one to gain appreciation of how the choice of both the formulation composition and the drying process parameters influence particle microstructure, and hence powder quality. In addition, an in-depth understanding of the key mechanisms leading to the formation of particles with different morphology/structure will aid the development of droplet drying and particle formation models that can be applied to spray dryers. For example, Abdullahi et al. [43], Handscomb et al. [44, 45] and Seydel et al. [46] developed models based on population balances and heat and mass balances to describe the evolution of the particle morphologies obtained from spray drying. In the light that the precise experimental conditions used in spray dryers are often not accessible in single droplet drying devices (as mentioned above: droplet size, heat/mass transfer rates, temperatures), these mechanistic drying models represent a promising avenue to transfer single droplet drying data to full scale spray dryer conditions. Although, in the existing works droplet drying kinetics for the systems considered were compared to experimental data, the structural properties of the particles obtained from the model were not validated with experiments due to a lack of adequate particle characterization approaches that allowed investigation of the properties of interest.

This contribution is therefore motivated by the gap in the literature and aims to further develop an understanding of the morphological evolution of droplets and to provide detailed microstructural information of particles obtained from single droplet drying experiments. The resulting dataset will allow for the development of accurate and robust single droplet model methodologies that will form the building block for the development of more robust spray dryer models. One must however take note that applying the general conditions from single droplet drying to spray drying is not straightforward due to the differences mentioned above. In addition, SDD studies do not capture interactions between droplets, particles and the chamber walls associated with spray drying. Understanding these differences is key to interpreting results from single droplet drying operations and applying this for the optimisation of spray drying processes. In the present contribution, we have applied XCT to elucidate the structure of particles obtained by acoustic levitation, and have uncovered a fascinating variety of structures; depending on the mixture dried (we have investigated combinations of different solutes

over a range of solid concentrations), as well as the processing conditions (temperature of the drying gas). Investigating the droplet drying kinetics and the resulting particle microstructure for a variety of mixtures and operating conditions enables one to gain deep insight into the process behaviour and the properties of the resulting particles. The results obtained are correlated with the formulation and process parameters used. Thereafter, the morphological results are compared to those from a spray drying process. The remainder of this paper is organised in the following way; Section 2 provides an overview of the physics of droplet drying. Section 3 describes the experimental approach used for single droplet drying studies and the methods used to qualitatively and quantitatively describe the drying kinetics and final structure of the manufactured particles. Section 4 provides a detailed discussion of the results. Relevant conclusions are made in Section 5.

2. Physics of droplet drying

The drying of solution droplets (containing a volatile component, for example water, and a non-volatile solid forming component) to form particles is a two-stage process. In the first drying stage, evaporation occurs freely from the surface of the droplet. The surface area of the droplet therefore decreases almost linearly with time as long as the environmental conditions remain the same. This leads to the supersaturation of the droplet with respect to the solute and causes the formation of particles within the droplet. In the latter phase of drying, the formed particles agglomerate to form a rigid particle shell, resulting in the droplet shrinkage to nearly stop. This discontinuity is referred to as the critical point in traditional drying and the size of the particle after this point remains constant as liquid now moves from within the droplet to the exterior through the interstices of the rigid particle shell. The drying rate now depends on the increasing resistance of the particle shell to the moisture transport, until drying is complete. Under extreme drying conditions, such as high gas temperature leading to boiling, the formed shell layer may crack, inflate or even explode (depending on the mechanical properties of the formed shell) due to the build up of vapor in the droplet core. This will lead to open shells with large cavities or even complete disintegration of the particles into fragments. The evaporation behaviour in such a system is therefore unpredictable [47–49]. The drying history until the formation of a rigid shell is known to determine the morphological evolution of a particle [8]. To describe the particle formation process, the drying history must be quantified to account for the evaporation or droplet shrinkage

behaviour and component redistribution within the droplet. Since the overall behaviour of the above processes results from the combination of convective and diffusive transport mechanisms, it is possible to quantify the relative magnitude of the drying mechanisms. Vehring et al. [50] showed from the analytical solution of the governing transport equation that the dimensionless Peclet number, Pe, defined as the ratio of convective to diffusive transport, can be used to describe the combined effect of convection and diffusion within the droplet and hence, provide insightful information about the resulting particle morphologies. The dimensionless Peclet number, Pe can be written as:

$$\mathrm{Pe}(t) = \frac{k(t)}{8D_{ij}(t)} \tag{1}$$

where $k(t)$ is known as the evaporation constant [1] and is given by:

$$k(t) = \frac{\mathrm{d}}{\mathrm{d}t}\left(d^2\right) = \frac{4\dot{m}_\mathrm{v}}{\rho\pi d} \tag{2}$$

d is the droplet diameter, t is time, $\dot{m}_\mathrm{v}$ is the evaporation rate and ρ is the liquid density. Several models exist for the calculation of the evaporation rate where experimental data is not available [51, 52]. The diffusivity D can be estimated from the Stokes-Einstein correlation for a binary system as [53]:

$$D_{ij}(t) = \omega_i \frac{k_B T_{wb}}{6\pi\eta r_{p,i}} + (1-\omega_i)\frac{k_B T_{wb}}{6\pi\eta r_{p,j}} \tag{3}$$

where i and j are the diffusing components, ω is the mass fraction, k_B is the Boltzmann constant, T_{wb} is the wet bulb temperature, η is the viscosity of the solution and r_p is the hydrodynamic radius of the respective molecule.

From Equation 1, a low Peclet number indicates that convective transport is low or comparable to the diffusive transport. In such a case, the concentration of the droplet remains close to uniform throughout the drying process, resulting in the formation of a rigid porous structure as shown in Figure 1. On the

[1] An expression relating the evaporation constant to the mass evaporation rate, $\dot{m}_\mathrm{v}$ of solvent from the droplet may be derived from a mass balance: $\dot{m}_\mathrm{v} = \rho\frac{\mathrm{d}V}{\mathrm{d}t} = \frac{\rho\pi}{6}\frac{\mathrm{d}}{\mathrm{d}t}\left(d^3\right) = \frac{\rho\pi}{6}\left[d^2\frac{\mathrm{d}}{\mathrm{d}t}\left(d\right) + d\frac{\mathrm{d}}{\mathrm{d}t}\left(d^2\right)\right]$. The change in the diameter of the droplet may be linked to the mass evaporation rate, assuming a spherical droplet by: $\frac{\mathrm{d}}{\mathrm{d}t}\left(d\right) = \frac{2\dot{m}_\mathrm{v}}{\rho\pi d^2}$ [51]. Combining these two equations, one obtains Equation 2.

other hand, a large Peclet number implies that convective transport dominates over diffusive transport (i.e., there is little time for the solute to diffuse inward from the surface). This behaviour typically results in the formation of hollow structures (Figure 1). Although the transport processes are important as above, particle formation itself is often a result of crystallisation in crystal forming systems, or gel formation in gel forming systems. It is therefore important to pursue a combined understanding of both the transport and particle formation mechanisms. The scope of this work is therefore to explore qualitatively and quantitatively the resulting transport processes ensuing from drying, and develop key understanding of the mechanism of particle formation.

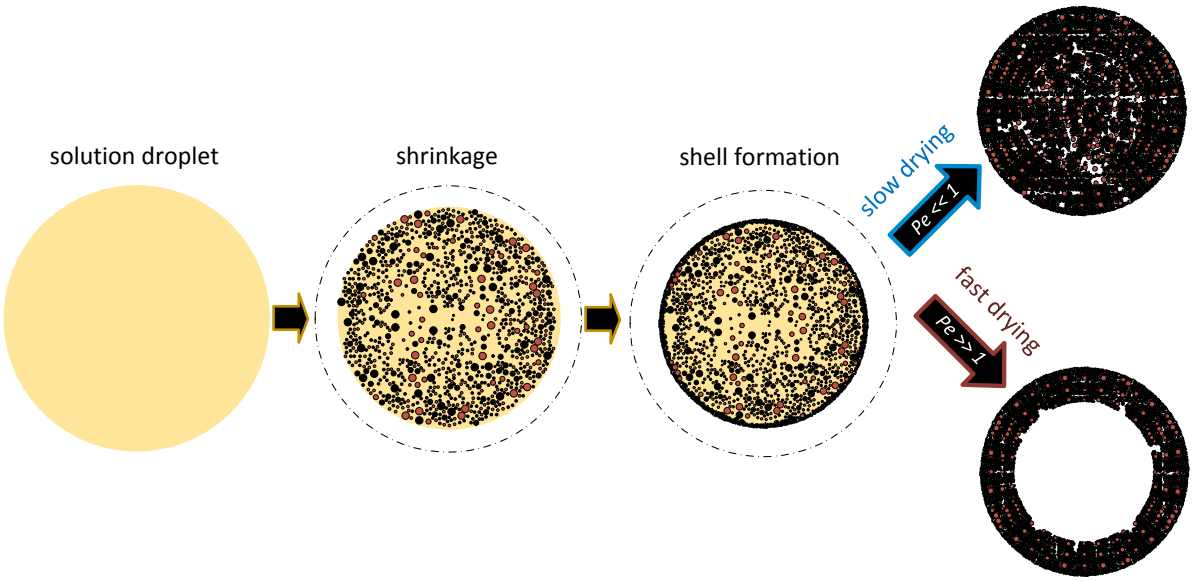

Figure 1: An example scheme of the morphological evolution of a droplet during drying. In this case, the drying process leads to the formation of a rigid porous or hollow particle. The range of particle morphologies obtainable is not limited to the above and depending on the drying condition and formulation, shrivelled or inflated particles may also be obtained [9, 44].

3. Experimental Method

3.1. Materials and sample preparation

The stable β form of D-mannitol was sourced from Alfa Aesar, with chemical purity >99%. Polyvinylpyrolidone PVP (10,000 g mol^{-1}) with chemical purity >99% was sourced from Sigma Aldrich. High purity deionised water with a resistivity of 19 MΩ cm was obtained from a Direct-Q3UV Merck purification system and was used to prepare stock solutions. Mannitol-water solutions at different concen-

trations were prepared in a 2 mL vial, where the mass of mannitol for the concentration range (0 - 11% w/w) was measured using a laboratory weighing scale (Mettler Toledo ML304T/00) with resolution of 0.1 mg. The mannitol was mixed with water and agitated continuously until complete dissolution was visually observed, typically after 5-20 minutes at room temperature. In the same way, ternary solutions containing PVP at different concentrations were prepared. Table 1 lists the samples used in the experiments conducted. Each experimental condition was repeated 3–4 times to ensure repeatability of the drying rates and particle morphologies[2]. Note the sample names describe the starting concentration and temperature for which the experiment was performed at. These names will be used for sample identification at several points in this work.

Table 1: A summary of the experimental conditions used for particle morphology and microstructure analysis [1] [2].

Sample	Mannitol (w/w%)	PVP (w/w%)	PVP fraction (w/w% solid)	Temperature (°C)	**Sample**	Mannitol (w/w%)	PVP (w/w%)	PVP fraction (w/w% solid)	Temperature (°C)
M1-60	0.9	0	-	60	P3-60	4.5	2.5	0.36	60
M5-60	4.5	0	-	60	P5-60	4.5	4.8	0.52	60
M7-60	7.3	0	-	60	P8-60	4.5	7.8	0.63	60
M11-60	11.2	0	-	60	P15-60	4.5	15	0.77	60
M5-40	4.5	0	-	40	P20-60	4.5	20	0.82	60
M5-80	4.5	0	-	80	P5-40	4.5	4.8	0.52	40
P1-60	4.5	0.9	0.17	60	P5-80	4.5	4.8	0.52	80

[1] All solutions (w/w%) were prepared from water as the solvent and using dry nitrogen as the drying gas. The molecular weight of PVP used is 10000 g mol^{-1}.

[2] Each investigated condition is repeated 3-4 times and the particles obtained at analysed morphologically.

3.2. Apparatus

The drying droplet is contained in a controlled environment flushed with dry gas at a defined temperature. The inner diameter and height of the cylindrical drying chamber is 70 mm and 140 mm respectively, giving a chamber volume of roughly 540 mL. The chamber is equipped with two sealable access windows of 25 mm diameter each to allow for the suspension of droplets and for optical imaging. The setup consists of a Tec5 ultrasonic levitator (100 kHz and maximum power output of 5 W),

[2]The experiments for each condition is averaged and the standard deviation of the drying rates and the particle properties defined was calculated. The results for this are given in Table 2, Table 3 and Table 4

an Allied vision manta G505B camera equipped with a telecentric lens, backlight LED illumination (Edmund Optics) and a controlled evaporator unit (Bronkhorst, CEM 202A) as illustrated in Figure 2 (An image of the actual experimental system is also shown in the supporting information). The levita-

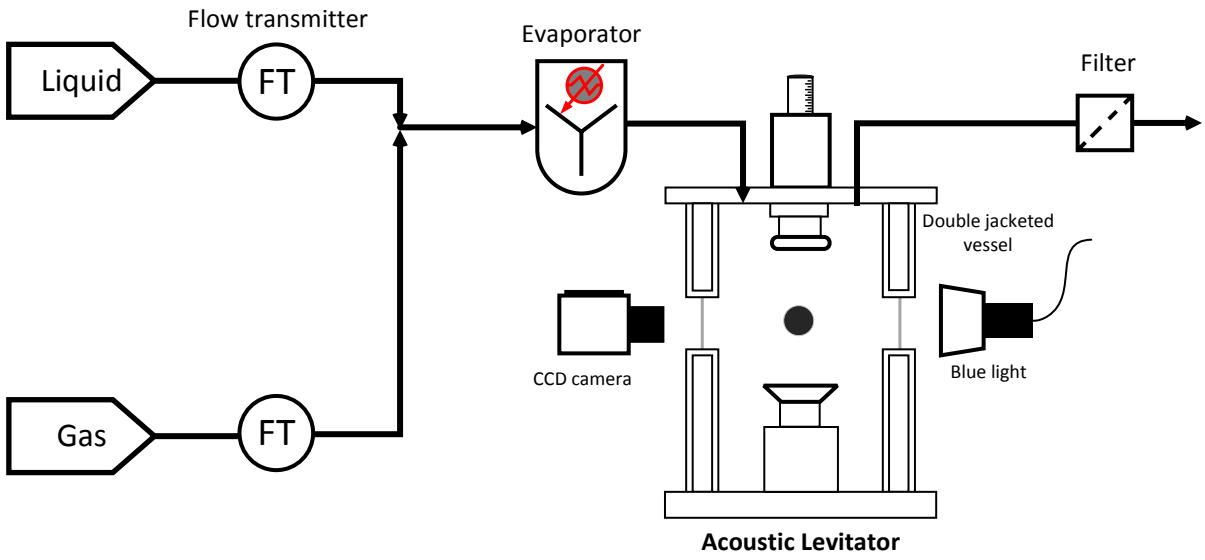

Figure 2: Scheme of the single droplet drying apparatus. This consists of a liquid tank and a gas cylinder, flow transmitters (FT), a controlled evaporator mixer, a temperature controlled chamber, a light and a camera to monitor the droplet drying history.

tor chamber is surrounded by a heating jacket for temperature control. The evaporator mixer is used to supply the chamber with a controlled gas flow at desired conditions (gas velocity, temperature, solvent saturation) by taking pure nitrogen gas from a gas cylinder. Note that the solvent saturation may be generated using the liquid flow stream. The resulting gas or gas mixture is sent to the evaporator, where it is heated to the desired gas condition and sent to the levitator. To ensure that the chamber is at the desired experimental condition, gas is allowed to flow through the chamber for a duration of 45-60 minutes before suspending a droplet. The flow rate of the gas is fixed at 1 L min^{-1} for all the experiments conducted (using a higher flow rate led to droplet instability in the acoustic field). This gives an average gas velocity of 0.04 m s^{-1}, based on the cross sectional area of the chamber. The gas employed in this study is set at 0% relative gas saturation throughout. The temperature and solvent saturation of the outlet gas was monitored using a thermochron ibutton sensor (DS1923) placed near the outlet of the chamber. This allowed the drying conditions to be followed continuously during drying. The change in the relative saturation of the outlet gas was found to be negligible throughout the experiments. By

conducting a mass balance around the chamber, we confirm that the change in outlet solvent saturation due to droplet evaporation is always less than 0.05% (cf. Sec. A in the supporting information). The droplet (typically 1.4 ± 0.1 mm) was suspended manually using a Hamilton 1800 model syringe. The power of the ultrasonic levitator was controlled from a power supply unit, starting with a power of between 0.45 – 0.5 dB (to allow for easy detachment from needle) to a fixed value of 0.32 dB (to keep the droplet stable after suspension). The droplet was visually observed following levitation from the continuous camera images to ensure that no visible bubbles were present at the onset of drying. This procedure ensured that any undesired condition that may uncharacteristically affect the final particle structure obtained was minimised.

3.3. Particle analysis methods

3.3.1. Optical imaging

The evolution of the droplet size was determined from the measurement of the projected droplet area using an image analysis algorithm developed in Matlab 2019a [43]. The droplet image was filtered (i.e., noise reduction algorithms were applied) and segmented. This was followed by the extraction of the major and minor axis of the projected droplet, assuming that the droplet was an ellipsoid with two of its three axes equal to the observed minor axis. From the ellipsoid's volume, an equivalent spherical diameter was calculated, allowing for the in-situ monitoring of the droplet during the drying process. The aspect ratio of the projected 2D image, AR = major axis/minor axis, was calculated and lies between 1 and 1.4 in all experiments (This is further discussed in section 4). The circularity, OC $= 4\pi\text{Area}/\text{perimeter}^2$, was also calculated and lies in the range 0.9-1 (see Figure S1 of the supporting information). This demonstrates that the assumption of droplet sphericity is reasonable. The critical point, describing the onset of morphology development was determined by the visual observation of the droplet during drying. For dense solids, the droplet becomes opaque, indicating a transition from a droplet to a semi-solid/particle. When the droplet diameter is plotted against time, shrinkage ceases as the droplet transforms into a rigid particle as expected. When the droplet diameter is fixed due to shell formation, literature presents precedents that still allow the drying process to be followed: either by monitoring the moisture content of the outlet gas [54] or by tracking the displacement of the particle from the sound pressure node [55]. The design of our evaporation chamber (large volume in

comparison to the droplet; motivated by a desire to keep drying conditions constant over time) and limited resolution of the moisture sensor made the former method inapplicable in our case. The latter was investigated for a few conditions in this work. However, data scattering, presumably induced by droplet/particle rotation in the acoustic field (which might be a result of the objects' heterogeneity), made the results unreliable for our purposes. The present work is therefore limited to tracking the drying rate up to the shell locking point, while all further characterization efforts (as below) focus on the final dried particles.

3.3.2. Scanning electron microscope

The particle morphology (shape, size and surface topology) was visualised using a high resolution scanning electron microscope (SEM). A Tescan Mira3 GMU VP analytical FE-SEM, with a working pressure of 0.1 Pa, a voltage of 5 kV and a power of 2 A was used. Samples were collected on a 12 mm circular disc covered with adhesive carbon tape and sputtered with conductive platinum (5-10 nm thickness; using Cressington sputter coater 108 system with MTM-20 thickness controller) to prevent the sample charging.

3.3.3. Raman spectroscopy

Raman spectroscopy was used to identify the crystallinity and polymorphic forms of the particles. A JY Horiba LabRam300 confocal Raman microscope equipped with a class 3B HeNe laser (632.82 nm) was used for the measurements. The spectrum was obtained using an objective of 100X in the Raman shift range 400 – 3500 cm^{-1}. To avoid any solid form transformation especially in the presence of moisture, samples were allowed to dry at the gas condition for up to 1 h after particle shell formation and before storage in sealable vials. Thereafter, Raman analysis was performed within a day of sample preparation. The laser was focused on 3-4 random points on the particle surface and the Raman spectrum obtained for each focused point was analysed to determine the polymorphic outcome since Raman spectroscopy is not a bulk measurement technique.

3.3.4. X-ray computed tomography (XCT)

XCT is an imaging technique that presents a way to non destructively visualise the internal microstructure of a 3D object. In XCT, X-rays are focused on an object. The object is rotated 360° and images are collected from different angles for 3D reconstruction. The incident X-ray beam passing through every volume element (voxel) of the object is attenuated with the degree of attenuation dependent on the density of the material and on its composition (elements with higher atomic number attenuate stronger). Since the samples analysed in this work consist of similar proportions of C, H, N and O, the composition effect is of low importance. The final intensity of the X-ray after absorption by the material is measured using detectors, providing direct image contrast. In this work, measurements were taken using a Zeiss Xradia Versa 250 with diffraction contrast tomography (DCT). Samples were imaged with a 10X objective lens, exposure time of 2 s, a voxel resolution of $(1.2\ \mu m)^3$, a field of view of 0.8×0.8 mm, a source energy of 120 kV and a power of 10 W, with each scan consisting of 1601 projections. To load the samples, each sample was adhered to a carbon tape and fixed on a small sample holder. Image reconstruction was performed using Zeiss XRM Reconstructor. The reconstructed data was further processed using a combination of Avizo software (FEI VSG, Thermo-Fisher) and a self-written code in Matlab.

3.4. 3D image processing and analysis

Images obtained from XCT were processed to obtain relevant microstructure information (size, porosity, shape etc.) of the 3D volume. Figure 3 shows exemplary images of the processing step of an XCT projection in the 2D X-Y plane. The first aspect of the image processing involve the identification of the region of interest with Avizo using a watershed algorithm, allowing for the separation of the particle from the carbon tape used to secure the particle. This was followed by the application of a median filter, ring artefact correction and beam hardening artefact correction where required (Figure 3a). The rest of the image processing steps were performed using Matlab. The functions used for analyses are highlighted in the discussion that follows. In the second step, an adaptive threshold was applied to the region of interest for segmentation from the background, using Matlab's 'graythresh' function [56]. This is illustrated in Figure 3b. In the final step, the connectivity of solids on each slice in 3D was established using the function 'bwconncomp', and the resulting volume space was rendered using the

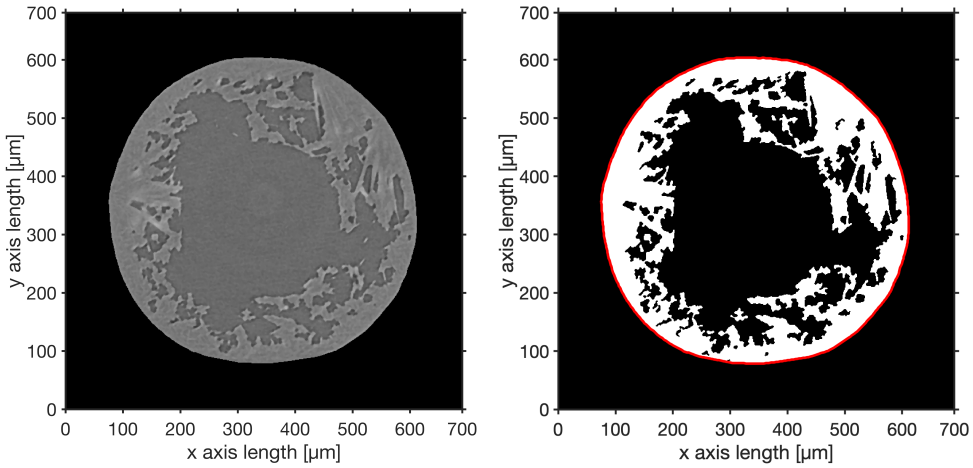

Figure 3: XCT image analysis procedure for the identification of the internal structure of a mannitol particle. a) gray scale image b) processed image with an enclosing boundary in red. Note that the white pixels represent the solids.

function 'isosurface'. This analysis allows the solids and pore spaces within each slice to be identified. The solid fraction, ε, of each slice is given as the ratio of the solid volume, $V_{\text{p,slice}}$, to the total volume of the slice, V_{slice}:

$$\varepsilon_{\text{slice}} = \frac{V_{\text{p,slice}}}{V_{\text{slice}}} \tag{4}$$

The resulting solid fraction distribution along the z-direction can be determined by computing the solid fraction for each slice.

Since the z-axis of the particle depends on the particle orientation and hence axis of rotation, it is necessary to make the computed solid fraction distribution independent of the axis of rotation. This was achieved by expressing the solid fraction as a function of the equivalent spherical radius of the particle (instead of a function of the z-axis). This allows particles obtained under similar conditions but with slightly different sphericity to be compared. By identifying thresholds or steps in the solid fraction distribution, this further provides information on the shell thickness of a particle (this will be discussed in further detail in the following). In the discussion that follows, we highlight a methodology that allows the solid fraction to be expressed as a function of an equivalent sphere radius. Consider the manufactured particles as onion like structures, with each onion layer representing a spherical shell layer. The solid fraction of each defined shell layer can be expressed as a function of the radial position within the particle, assuming it is a sphere.

The first step starts with finding the enclosing boundary of the particle. The boundary was defined as the convex hull, 'convhull(I)', of the object, I, when they contain a blow hole, otherwise the actual boundary of the object, 'bwboundaries(I)', was computed when a blow hole does not exist. Ideally, this type of analysis should be performed using the actual boundary of the particle slices. However most particles obtained in this work possess a blow hole that exposes the interior of the particle to the exterior. The consequence of this is that in some of the slices the boundary is not closed cf. Figure 4a. In order to avoid this problem and make the analysis consistent, it was necessary to use the convex hull approximation to close the boundary for each slice. In the case of shrivelled particles, the blow holes do not exist (a consequence of the formulation and drying condition) and therefore the convex hull approximation was not required, an example of this type of particle is illustrated in Figure 6b, where the volume space has already been rendered (2D slices of this particle are shown in the supporting information, Figure S3). Hence, the choice of algorithm depends on the nature of the particle. In the next step, the convex hull of the object in each layer was masked, 'imfill', (Figure 4b). The layers were then combined to create a 3D masked (filled) volume of the original particle (i.e., the particle volume was reproduced assuming no void space exists). Each pixel of the now masked particle was then mapped to its outer boundary by calculating the euclidean distance transform in 3D i.e., each non zero (white) pixel is mapped to the nearest zero (black) pixel which represents the outer boundary of the 3D masked volume, 'bwdist'. The white pixels were binned based on the distance from the outer boundary into defined particle shell layers accordingly. Figure 4c illustrates a cross section of the 3D distance transform of the particles (note that this is a 2D cut view of the 3D transform of the particle at the same z position as the binary images).

The mapped layers from the 3D distance transform of the masked image were used to produce the shell layers in the original particle (onion layers as mentioned above). Figure 5a and Figure 5b show the 3D cross sections of the constructed shell layers for the masked and original particles respectively. One can observe that the hole present at the surface is now closed when the particle is masked as expected. Figure 6a and Figure 6b shows the constructed shell layers when the particle of interest is collapsed or shrivelled. In this case, the convex hull approximation is not required and the actual particle boundary is used to produce the shell layers. The shell layers are then transformed to fit in a sphere equivalent particle, i.e., the volume of each spherical layer has the same volume as the corresponding shell layer

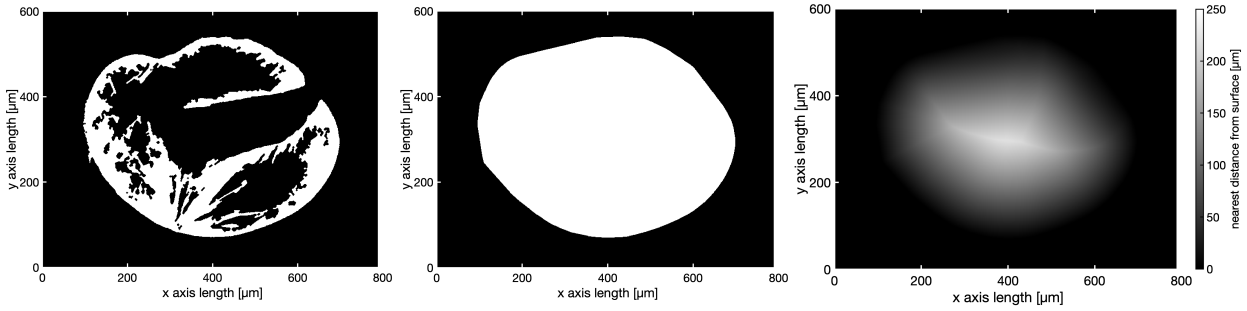

(a) (b) (c)

Figure 4: a) segmented image of a particle slice b) masked (filled) image of a particle slice c) distance transform of the cross section of a particle (obtained from its 3D distance transform).

in the original particle. The thickness, δ_r, of a spherical shell layer, k, is given by:

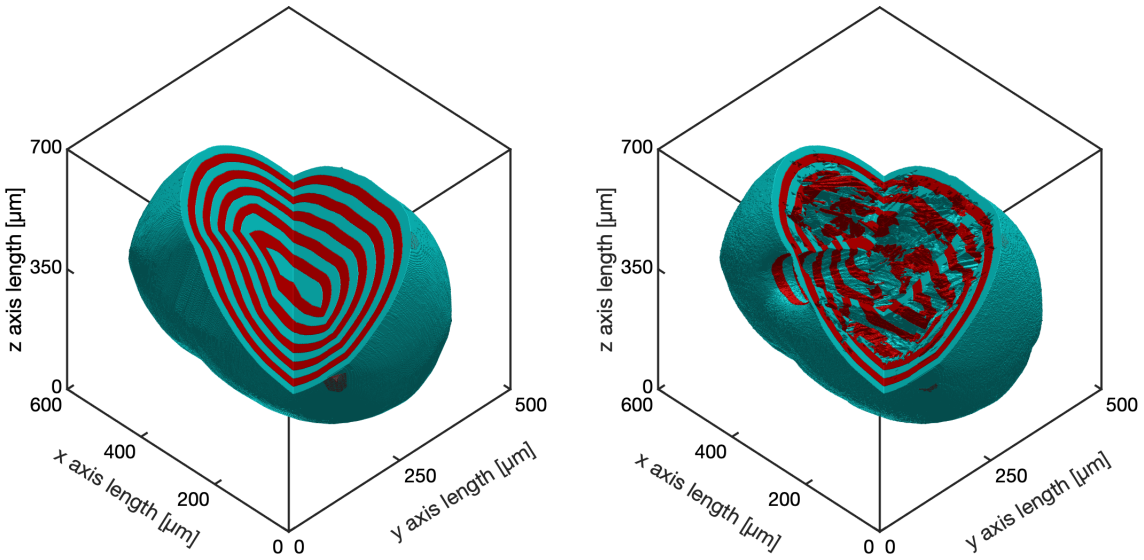

(a) (b)

Figure 5: 3D rendering of a particle showing its shell layers a) an ideal particle without voids i.e., with 100 % solids. Note that this is an actual particle obtained from experiments, but in this case the particle is masked b) original particle with voids as obtained experimentally. Each shell layer is 15 µm thick.

$$\delta_{r,k} = r_{o,k} - r_{i,k} = r_{o,k} - \left(r_{o,k}^3 - \frac{3}{4\pi} V_{\text{shell},k} \right)^{\frac{1}{3}} \tag{5}$$

where $r_{i,k}$ and $r_{o,k}$ is the equivalent inner and outer radius of the spherical shell layer, k, respectively and $V_{\text{shell},k}$ is the volume of the shell. The solid fraction distribution of the particle can be plotted as

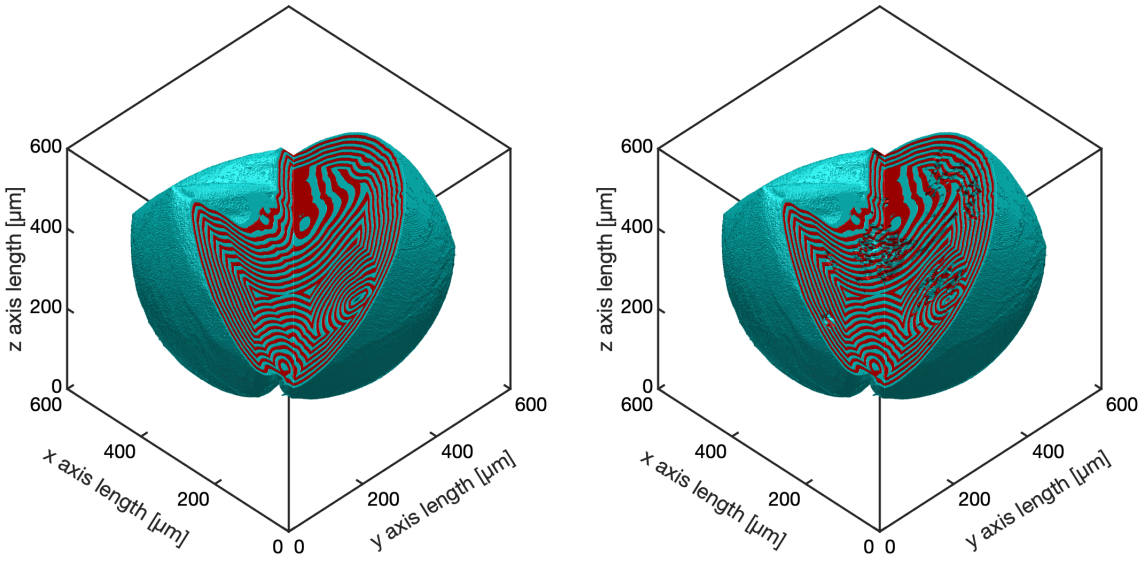

(a) (b)

Figure 6: The 3D the rendering of a deformed particle showing its shell layers a) voidless particle with a solid fraction of 1 and b) original particle with small amount of void space. The thickness of each shell layer is 10 µm.

a function of the equivalent sphere radius, r, of the particle. The thickness of the shell layers within the particle (based on the mapped distances) can be chosen as a parameter of analysis. For example in Figure 5, the chosen shell layers are 15 µm thick. However, the region of the actual particle that is classified as a shell (usually the region with a high solid fraction) requires a predefined criterion to define the particle shell region and hence its thickness.

In the ideal case shown in Figure 1 where the particle is symmetrical, identifying the shell region is straightforward since a plot of the solid fraction, or cumulative solid fraction will indicate a sharp rise at the inner boundary of the particle shell region. The particles obtained in this work are non symmetrical and the shell region is similarly not symmetrical. In Figure 5b, there exists a region of minimum and maximum shell thickness. It is therefore counter intuitive to define a specific average shell thickness value. Instead, the shell region is defined based on several criteria. The minimum shell thickness is defined as the region of the shell with a solid fraction, ε, of at least 0.7, while a maximum shell thickness is defined by the region of the particle with a solid fraction of at least 0.5. It is also possible to quantify the thickness using the cumulative solid fraction, since ideally the shell region will hold a

considerable amount of the total particle solid content. The cumulative solid fraction is given by:

$$C_{sf}(k) = \frac{\sum_{i=1}^{i=k} V_{p,shell}(i)}{\sum_{i=1}^{i=n} V_{p,shell}(i)} \tag{6}$$

where $C_{sf}(k)$ is the cumulative solid fraction of solids, starting from the centroid of the particle to shell layer k, and n is the number of shells. In this case, the minimum and maximum shell thickness is defined as the region containing at least 50% or 70% of the total particle mass respectively.

Comparison between the thickness defined using the above methods is discussed in the result section, Section 4. Figure 7 shows an example of the cumulative solid fraction and the solid fraction distribution for the particle depicted in Figure 5. The solid fraction in this plot is seen to decrease starting from the

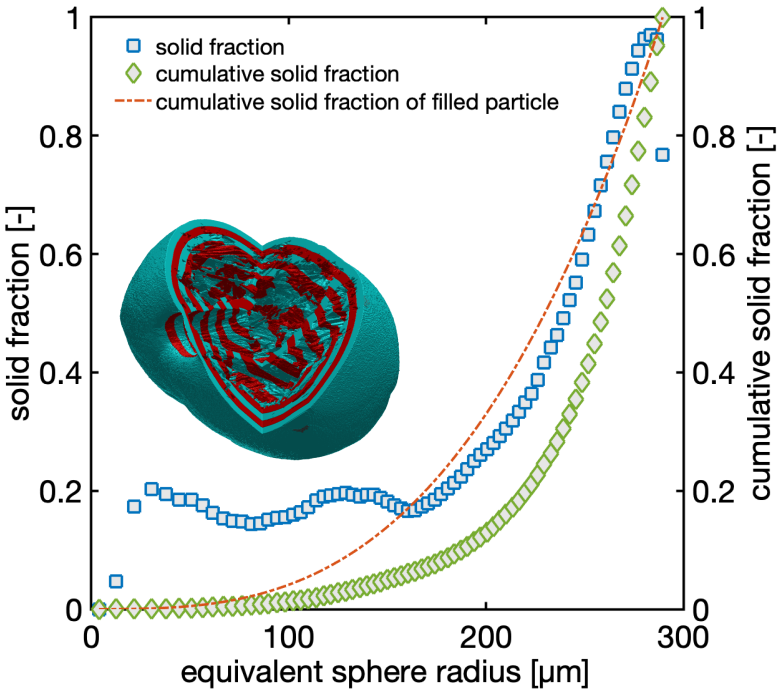

Figure 7: Profiles of the solid fraction and the cumulative solid fraction for the particle shown in Figure 5b.

surface until a minima is reached, usually zero in the case of a hollow particle. In extreme cases where several minima exists as consequence of the architecture of a particle, the thickness value is taken as that before any minima, i.e., the thickness is defined as the region where the solid fraction, starting from

the surface first drops below the predefined values. This kind of behaviour is probable particularly in completely deformed (shrivelled) particles such as Figure 6b (the profile for this is shown in Figure S4 of the supporting information). In the case of the cumulative solid fraction, this consideration is not relevant since the distribution is monotonic. Comparing the cumulative solid fraction of a voidless particle to the original particle (Figure 5), one can clearly see that a considerable amount of solid is contained in a small region close to the surface.

4. Results and Discussion

4.1. Droplet drying behaviour

During the evaporation of a pure component droplet, there is no internal limitation to mass transport and evaporation proceeds through a period of ideal shrinkage. At the beginning, the temperature of the droplet changes gradually to the wet bulb temperature of the liquid and remains constant at this temperature for the remaining duration of drying. According to the d^2 law [52], the plot of the normalised surface area against time should be linear in this regime for pure substances. Figure 8a shows the drying profile for water (averaged for five different set of experiments). The surface area of the droplet is observed to decrease almost linearly with time accordingly. The slight deviation from linearity is rationalised to be the effect of decreasing Reynold's number as the droplet shrinks, an effect that is considered negligible in the derivation of the d^2 law [43, 52] cf. Figure S1 of the supporting information in Abdullahi et al. [43]).

During drying, the droplets were observed to be deformed. The droplet deformation can be represented by the aspect ratio as shown in Figure 8a. One can observe that the droplet aspect ratio decreases to a value of 1.0 as the droplet size decreases over time. This effect is well documented in literature and has been explained to be a result of the non-uniform sound pressure distribution around the droplet in the acoustic field [55, 58]. The extent of deformation depends on the size of the droplet, droplet properties (surface tension of the liquid) and the sound pressure. The sound pressure distribution also leads to the streaming of the gas. This gas streaming affects the convection of solvent vapour away from the droplet surface. In primary acoustic streaming the droplet will experience enhanced convection while in secondary acoustic streaming, the convective transport is reduced. Generally, one can reduce or

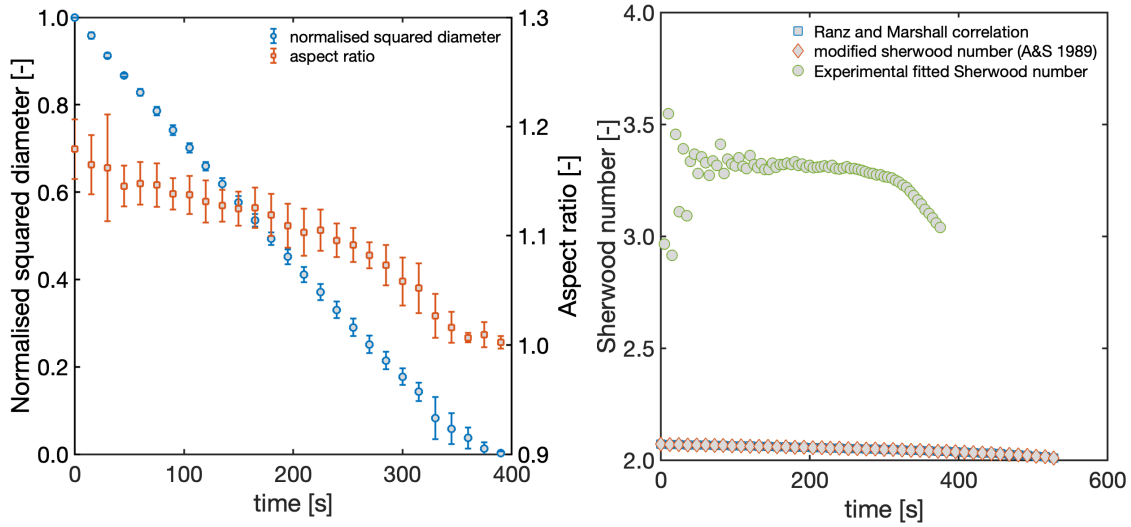

Figure 8: a) The drying profile of water evaporated at 60°C, 0% relative gas saturation and a gas flow rate of 1 L min^{-1}. The data presented here is averaged for five different experiments. b) Sherwood number for evaporation predicted according to the Ranz and Marshall [57] correlation and Abramzon and Sirignano [51] and compared to that obtained from acoustic levitation experiments for a single experiment.

eliminate these effects by blowing a gas around the droplet [59, 60]. In order to understand the effect of acoustic streaming on mass transfer, one can approach the problem by computing the time evolution of the Sherwood number during evaporation in an acoustic levitator, and compare this to theoretical values. We have explored two mass transport approaches to predict the Sherwood number for evaporation: 1) the Ranz and Marshall [57] correlation and 2) the modified Sherwood number detailed by Abramzon and Sirignano [51]. To determine the actual Sherwood number, one can use the d^2 law for evaporation under forced convection, as described by Tuckermann et al. [61] and fit this to the drying profile:

$$r^2(t) - r_0^2 = -\frac{2D_v M}{\rho_s R}\left(\frac{p_{\mathrm{wb}}}{T_{\mathrm{wb}}} - \frac{p_\infty}{T_\infty}\right)\frac{\mathrm{Sh}(t)}{2}t \tag{7}$$

where D_v represents the vapour diffusivity, M is the molecular weight of the solvent, p_{wb} is the saturated vapour pressure computed at the wet bulb temperature, T_{wb}, of the droplet surface, p_∞ is the vapour pressure at the bulk gas temperature, T_∞, and is lower than p_{wb} and Sh is the Sherwood number. Note that the value of p_∞ is zero for a dehumidified gas. The temporal evolution of the Sherwood number is shown in Figure 8b for a single drying profile of water. The maximum Sherwood number is observed at 3.6 and is substantially larger than the value of 2.0 for evaporation in quiescent gas, as

well as for evaporation under forced convection without any sound influence. The results clearly shows the influence of acoustic streaming on the evaporation of droplets in an acoustic levitator. These effects do not prevent comparing single droplet drying experiments carried out with acoustic levitation to pilot/full-scale spray drying experiments, but should be noted (i.e., rather than matching gas velocities directly, one should match the Sherwood number occurring in both experiments (while also matching the remaining experimental conditions)).

In a solution droplet where two main drying regimes exist, drying during the first stage is unhindered similar to the drying of pure water. In the second stage, the formation of a shell or skin layer at the surface creates a resistance to mass transport as internal moisture migration becomes the rate limiting process. The rate of evaporation therefore decreases significantly. The drying behaviour of the solution

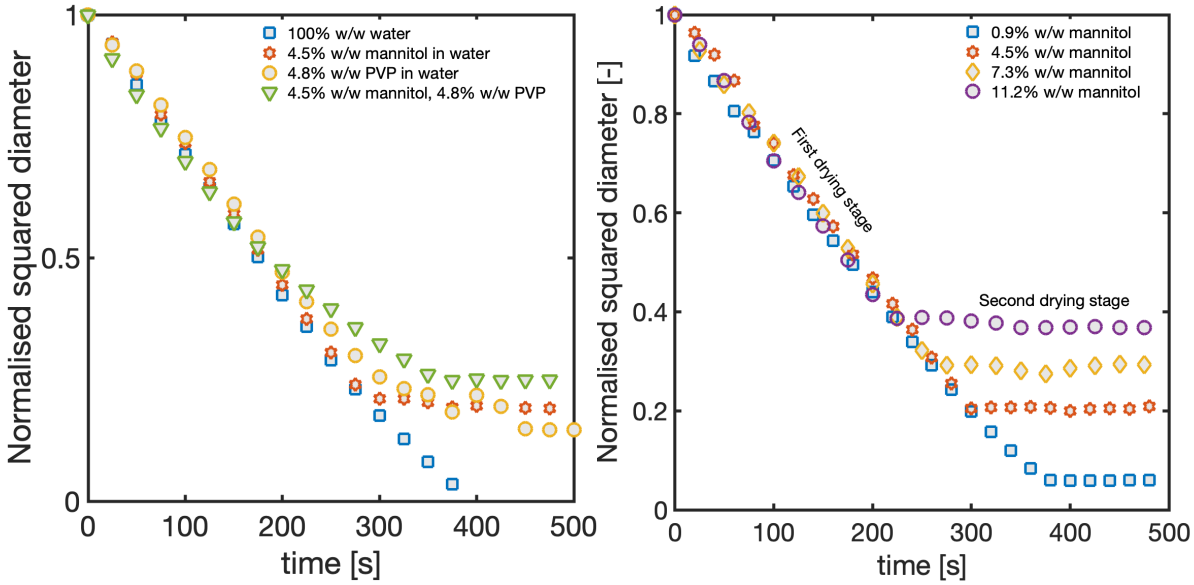

(a) (b)

Figure 9: a) The drying behaviour of aqueous solution droplets containing mannitol, PVP and mannitol-PVP and b) the effect of the starting concentration of mannitol on the drying behaviour of solution droplets. All experiments were conducted at 60 °C, 0% relative gas saturation and a gas flow rate of 1L min $^{-1}$.

droplets containing mannitol in water, PVP in water and mannitol and PVP in water are compared in Figure 9a [3]. The result illustrates a reduction in the evaporation rate during the first drying stage for

[3]The drying history of all solution droplets was seen to be repeatable by conducting 3 experiments at the same conditions and the average evaporation constant $\left(\frac{\Delta d^2}{\Delta t}\right)$, as well as the standard deviation are summarised in Table 2, Table 3 and Table 4.

solutions containing mannitol and PVP when compared to pure water. This may be attributed to the reduction in water activity due to the presence of other species in the solution, leading to a reduction in the partial pressure exerted by the solvent. At the onset of the second drying stage, the solution droplet forms a shell as a result of solid agglomeration or gel formation at the droplet surface. For these experimental conditions the particle size remains constant for the remainder of the drying period.

In the case of aqueous PVP solutions, the formation of a sticky gel was observed (when collected on a spatula a few minutes after the critical point) but when allowed to dry for several hours, the solid becomes non-sticky as the moisture content of the particle is reduced significantly. The drying of PVP-water and mannitol-water solutions is further observed to exhibit comparable drying times until the critical point, Figure 9a. Figure 9b shows the drying kinetics of mannitol-water solutions for different initial concentrations. It can be observed that during the first drying stage, the drying rate is almost independent of the mannitol solution concentration. However, as the concentration of mannitol increases, the critical point occurs earlier due to increased crystal nucleation and growth kinetics resulting from the larger concentration gradient driving force.

4.2. Effect of starting solution concentration on particle structure

The dried particles collected at the end of the drying process were analysed using the range of techniques discussed in Section 3. SEM images of mannitol particles obtained at different starting concentrations are shown in Figure 10. The external morphology illustrates the tendency of mannitol to form needle-like crystals [62]. The most distinct features observed are the particle size, the presence of holes in the shell of the particle and the surface roughness.

The SEM images show qualitatively, the increase in particle size with increasing starting concentration (scale bar is 200 μm in all images). This is also demonstrated in the droplet drying history shown in Figure 9b. As discussed in Section 2, the evaporation of solvent from a solution droplet causes an increase in the solute concentration at the surface as the droplet shrinks. The high concentration at the surface is then transported by diffusion towards the centre of the droplet. When the concentration exceeds the saturation concentration of the solute in the solvent, the system is said to be supersaturated and a driving force for crystallisation is established. This leads to the nucleation and growth of crystals

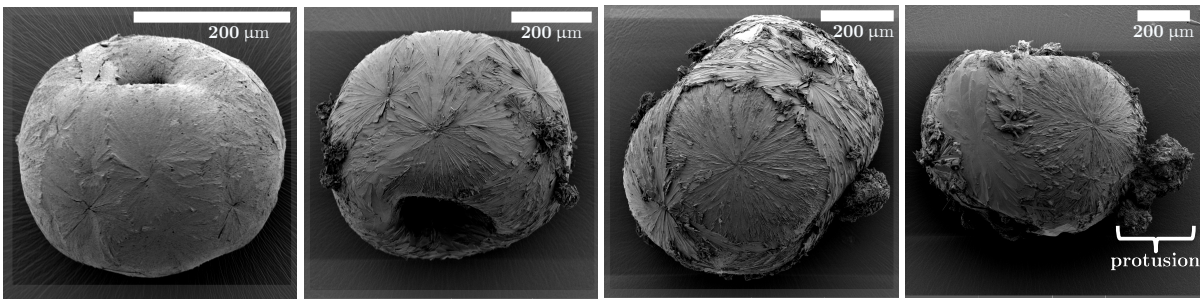

Figure 10: Scanning electron microscope (SEM) images of mannitol particles for different starting concentrations M1-60, M5-60, M7-60, M11-60 respectively.

in the solution droplet. The higher the starting concentration of the solute in the droplet, the higher the maximum concentration that can be reached at the surface during the drying process and the faster supersaturation is established. The effect of this is the earlier formation of a shell when the volume of the droplet/particle is still large. The effect of concentration is also reflected in the Peclet's number which relates evaporation to diffusion (Equation 1). The higher the starting concentration, the higher the concentration gradient between the droplet surface and the droplet centre and the lower the resulting Peclet number. This would be expected to lead to smaller particles due to the faster diffusion but this is also counteracted by the faster particle formation kinetics.

After a shell is formed, the evaporation of the solvent will continue through the interstices of the formed porous shell by diffusion or capillary transport. The slow transport mechanism in this regime may lead to the build up of pressure inside the particle since the formation of the shell now fixes the size of the particle and this may lead to particle rupture or collapse. The extent of this behaviour of course depends on the material make-up of the shell and the thickness of the newly formed shell. In the case of drying mannitol from aqueous solution, there is only one solute and shell formation is thereby driven by the solid formation kinetics of the single solute. Figure 10 shows the presence of blow holes in the shell for the concentration range investigated. This shows that the pressure build up caused by the volume expansion resulting from the formation of vapour within the droplet is enough to cause permanent deformation of the particle, starting from the weakest point i.e., the region with minimum shell thickness [19, 63]. In some cases, the shell collapses from two sides to form a toroid-like particle. At temperatures above the boiling point, the effect is expected to be more pronounced. However, such

conditions were not investigated in this work.

Although the physics described above are sound, it may be argued that the formation of the blow holes is attributed to the effect of the acoustic pressure. Pathak and Basu [63] however showed from the study of the buckling dynamics of droplets in an acoustic levitator that the capillary pressure observed during drying is an order of magnitude higher than the acoustic pressure observed. A qualitative comparative analysis of the result described above for mannitol to that obtained from lab and pilot scale spray drying experiments [64, 65] show very good comparisons and partially demonstrates that the presence of the instabilities may be common driving factors. In both spray dryer scales, particles with indents were obtained when drying at $60 - 70\ ^{\circ}C$, although the starting concentration used for the experiments was higher, at 15% w/w. The indents shown at these conditions rather than complete blow holes may be explained by the size of the particles formed in the dryer. The initial droplet sizes employed in the spray drying experiments were between one and two orders of magnitude smaller than that employed in this work. This led to the formation of much smaller particles and since smaller particles are expected to have a higher resistance to shell deformation for the same shell thickness, the difference in the extent of deformation can be qualitatively rationalized. Nevertheless, the analysis above show similar particle morphology to that obtained from spray drying experiments.

The surface roughness of particles is also seen to increase with increasing concentration. At low concentrations, the particles are observed to be smooth and as the concentration is increased, the degree of surface roughness increases. This can also be explained by the higher degree of supersaturation reached at higher concentrations, resulting in rapid nucleation and growth of crystals. The roughness of the surface is seen to originate from the presence of nucleation sites at the external surface of the particles from which crystals grows outwards on the surface during the drying process. At low concentrations, the number of surface nucleation sites is small and cannot be seen at the given resolution but as the concentration increases, the nucleation sites become more visible. From the results above, one can postulate that the presence of multiple surface nucleation sites may lead to the formation of rough structural features at the surface of the particles. The extent of this will depend on the combination of the drying kinetics and the kinetics of crystallization.

3D volume rendering from tomography measurements allow further visualisation of the internal mi-

crostructure of the particles. From the 3D rendered volume of the particles shown in Figure 11, needle-like crystals can be seen to propagate inwards from the surface, acting as supporting structure for the near spherical particles. The needle crystals in the particle interior are typically larger than the crystals

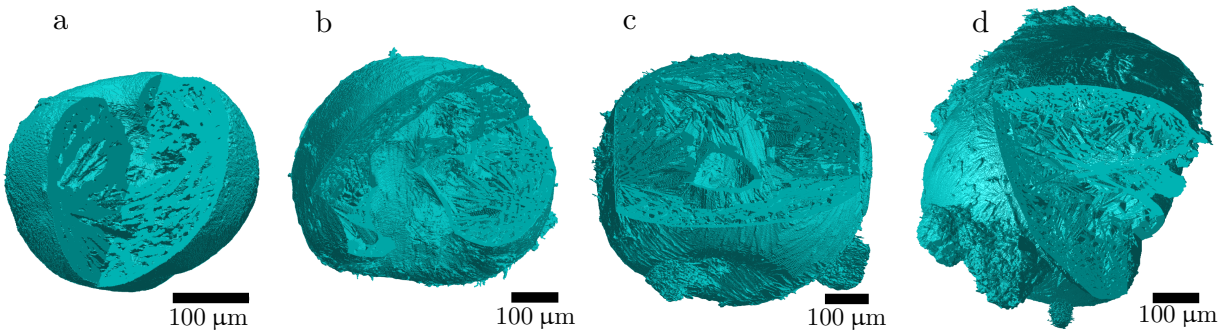

Figure 11: 3D volume rendering of particles obtained from the drying of aqueous mannitol solution at different concentrations a) M1-60 b) M5-60 c) M7-60 d) M11-60.

on the surface owing to the fact that the crystals in the interior are exposed for longer in the supersaturated solution as the solvent evaporates slower following shell formation. In the presence of a hole at the surface at high concentrations, crystals are seen to propagate outwards through the pores/holes to form protuberances on the particle surface. The presence of these protuberances leads to a decrease in particle sphericity as shown in Figure 12. The large error bars here can be explained by the difference in the extent of the formation of the protuberances.

From Figure 11, one can also observe that the particles are highly porous. We conducted a quantitative analysis of the particle porosity based on 1) the 2D projected area of particles obtained from the camera [4] and 2) the volume data from XCT as shown in Figure 12. The porosities calculated from the camera do not match with the XCT values, since the approximated volume of the final particle is larger than the actual. However, Tran et al. [66] observed a similar trend. Although the authors [66] showed that the calculated porosities were lower than expected, this may be attributed to the different method employed to approximate the final volume of the particle from the camera images [5]. Despite the above fact, porosities calculated from the camera images can provide valuable information where expensive

[4]The porosity was calculated as: $1 - \varepsilon = 1$ - volume of dense solid/volume of particle. The volume of particle in this case was calculated using the equivalent spherical diameter obtained from the camera.

[5]Tran et al. [66] have calculated the volume of the particle from the camera images, assuming the projected area is that of a sphere, rather than that of an ellipsoid as shown in the present work

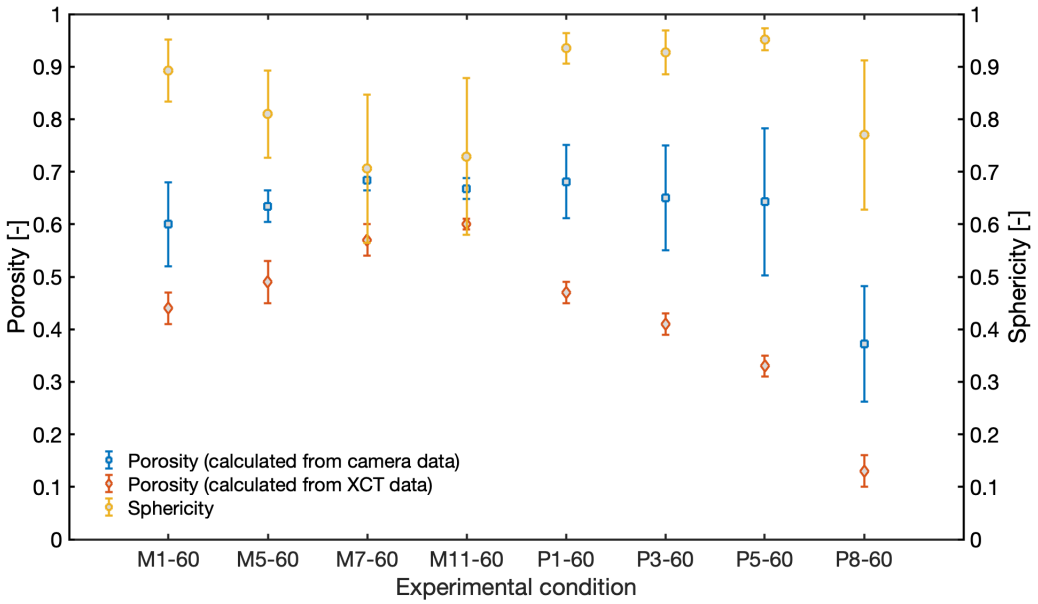

Figure 12: The effect of formulation condition on the porosity and sphericity of particles.

methods such as XCT are unavailable. One must however take care when calculating the porosity from 2D camera images as the computed volume depends on the projected area of the particle, which might differ according to the particle rotation. In addition, the particle vibration (due to the acoustics) may result in a blurry image, which leads to overestimation of the projected area.

Properties of the particle (size, sphericity, porosity and shell thickness) are summarised in Table 2. The thickness of the particles remains similar for the range of concentration investigated. A quantitative analysis of this using the solid fraction distribution shows that indeed this is true. However, a similar analysis based on the cumulative solid fraction of the particle shows that the thickness increases with the concentration of mannitol. This effect may be rationalised by the size of the particles. For example, an increase in the radius of the particle, $r_k + \Delta r_k$, leads to an increase in the volume of the outermost particle shell, $(r_k + \Delta r_k)^3$. However, the increase in solid fraction in the shell is not proportional to the increase in the shell volume due to the needle like behaviour of the crystals. This implies that the mass of solid decreases as one moves away from the surface. Therefore, the higher the starting concentration of mannitol in the droplet, the larger the particle, and the thicker the shell that is required to contain a given mass of the solid i.e., 50% or 70% as described previously [6]. One can observe the presence

[6]The crystals propagate inwards from the surface so that an increase in the size of the particle will mean that existing

of a hole located centrally within the particle shown in Figure 11c. This hole may be attributed to the existence of the blow hole which extends from the surface towards the centre of the particle.

The crystallinity of the particles was investigated using Raman spectroscopy. For the pure crystalline forms, characteristic peak positions were used to differentiate the solid forms. Fronczek et al. [67] and Cornel et al. [68] reported three anhydrous polymorphs of mannitol, β (stable), α (metastable) and δ (least stable) for the range of conditions considered in this work. According to Su et al. [69], the difference in peak centre positions and broadness for the bands centred at 480, 885 and 1123 cm^{-1} and band range 2850-3000 cm^{-1} can be used to differentiate the polymorphs. The first three plots in Figure 13a show an example of the difference in peak positions for the band range 2850 - 3000 cm^{-1} (dashed box) for the reference patterns [7]. The remaining spectra in Figure 13a are for the particles formed from mannitol-water solutions. For the range of concentrations of mannitol in water, M1-60 (0.9% w/w) to M11-60 (11.2% w/w) investigated, the α form was readily obtained at concentrations less than M7-60 (7.3% w/w), although traces of the stable β form were observed to form concomitantly for the concentrations M5-60 and M7-60. At a higher starting concentration M11-60 (11.2% w/w), the degree of concomitant crystallisation was observed to increase significantly, with the β form seemingly dominating the formed particle. A detailed result of the polymorphic outcome for different samples and sample points are shown in Table S1 of the supporting information. The concomitant crystallisation of mannitol has been previously reported [70, 71] and was explained to be a result of the competing nucleation and growth rate of the polymorphs.

As discussed in Section 2, the morphology and microstructure of the particles may result from the drying history of the droplets. This is related to the Peclet number, Equation 1. In non-ideal mixtures, the effect of solute concentration on the evaporation of solvent from the droplet can be significant, hence the degree of solvent flux and the diffusivity of the solute from the droplet surface towards the centre is a function of time. In our previous work [43], we have detailed a numerical solution to the conservation equations describing the drying history for the cases shown in the present work. From the simulation, we have solved for the evolution of the concentration profile over time. We have used results

crystals can grow further inwards from the surface. The small crystals acting as binders at the surface do not extend down from the surface.

[7] The reference patterns were obtained experimentally from pure samples.

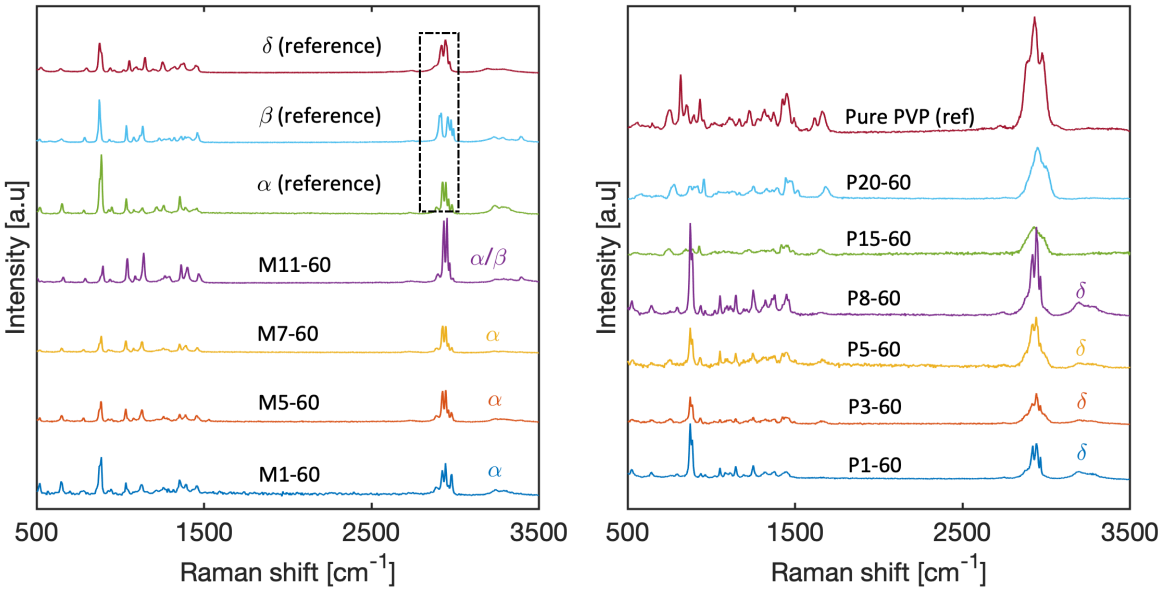

Figure 13: Raman spectra showing: a) the effect of starting mannitol concentration b) the effect of starting PVP concentration on the crystalline nature and polymorphic outcome of manufactured particles.

from the simulation to compute the Peclet number as a function of time. Our investigation showed that by normalising the Peclet number with the initial Peclet number for the formulation and drying conditions considered here, the data will collapse to a single profile. Such an analogy indicates the strong dependence of the Peclet number on the initial condition so that we can utilise the initial Peclet number Pe(0) to describe and compare different particle properties (see Figure S5 of the supporting information). The Peclet number calculated for each run is given in Table 2 and is seen to decrease with concentration as expected. The intermediate range of Peclet number (Pe $\approx$ 1) obtained throughout may demonstrate why rigid porous particles were obtained.

Table 2: Experimental results for the drying of mannitol solutions from different starting droplet concentrations [a].

Description	M1-60	M5-60	M7-60	M11-60
Evaporation constant k [10^{-9} m^2 s^{-1}]	4.96 ±0.2	5.18 ±0.2	5.24 ±0.2	5.18 ±0.2
Peclet number [-] [b]	0.95	0.94	0.92	0.87
Final particle size [µm]	325.6 ±12.4	552.8 ±5.5	693.6 ±19.8	802.9 ±27.5
Final particle porosity [-]	0.44 ±0.03	0.49 ±0.04	0.57 ±0.03	0.60 ±0.01
Sphericity [-]	0.89 ±0.06	0.81 ±0.08	0.72 ±0.14	0.73 ±0.15
Shell thickness with $\varepsilon > 0.7$ [µm]	6.8 ±2.1	6.5 ±0.1	6.8 ±1.0	- [c]
Shell thickness with $\varepsilon > 0.5$ [µm]	27.5 ±13.0	21.1 ±6.0	25.5 ±2.0	- [c]
Shell thickness with $C_{sf} > 0.5$ [µm]	18.6 ±1.6	34.0 ±1.9	36.01 ±0.7	40.2 ±1.6
Shell thickness with $C_{sf} > 0.3$ [µm]	32.6 ±2.4	59.7 ±2.3	67.0 ±0.7	74.5 ±2.1

[a] A gas flow rate of 1 L min^{-1} was used (determined from parameter fitting see Abdullahi et al. [43]) and a gas relative saturation of 0% in all investigations

[b] The Peclet number was calculated using Equation 1.

[c] The current method of analysis is still unable to accurately describe very rough particles as in the case of high concentration of mannitol due to the protuberances formed at the surface of the particle. However, it is possible to still quantify the cumulative solid of solids within the droplet with good accuracy.

4.3. Effect of polymer concentration on particle structure

To further understand the effect of formulation properties on the particles formed, different concentrations of PVP (a polymeric binder) were added. The particles obtained at the end of drying show qualitatively similar morphologies (with indents/blow holes at the surface) for low to medium concentrations (Figure 14). The particle is seen to transition from partially deformed (with blow holes) near spherical particles (P1-60, P3-60, P5-60) to a completely deformed (shrivelled) particle at high concentrations ≥ 7.8% PVP (P8-60). The shape of the particle is described by its sphericity and is shown in Figure 12. At low concentration of PVP relative to mannitol, mannitol precipitation is still significant and hence, the formed shell layer still possesses sufficient rigidity that prevents it from collapsing.

At high polymer concentrations relative to mannitol, the shell layer is increasingly dominated by the skin forming polymer and the forming shell is elastic, such that it collapses quickly due to the pressure forces acting on the shell. In the end, the strength of the final particle shell is influenced by the combination of mannitol solid precipitation and the polymer skin formation. The particles obtained show

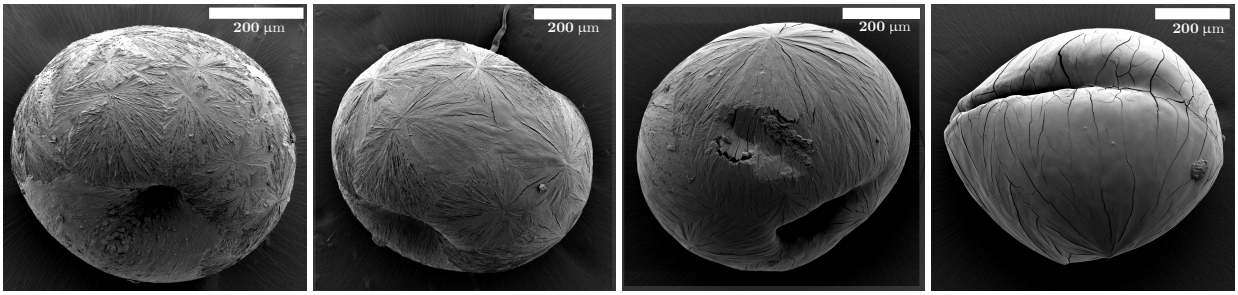

Figure 14: Effect of PVP concentration on a 4.5% w/w mannitol solution, from left to right P1-60, P3-60, P5-60, P8-60 respectively

smoother surfaces when compared to the binary case of mannitol in water shown in Figure 10. The addition of a skin forming material like PVP acts to inhibit the crystal formation kinetics of mannitol by trapping the solute molecules in the amorphous excipient matrix during solidification.

At low PVP concentrations, the effect of this inhibition mechanism is low, however as the concentration of PVP is increased, the effect of the polymer excipient dominates during the solidification process. The inhibition of crystallisation, coupled with the relative transport mechanism of the solutes (mannitol and PVP) determines the inception of shell formation and the smoothness of the particles. The results confirm that even at low polymer concentration, the particles are smoother when compared to the binary case M5-60 (Figure 10). However, this does not necessarily mean that the surface is solely the polymer as it may still consist of the crystalline mannitol.

In a multicomponent system such as this, the diffusivity of each component is affected by that of the other components. The faster diffusing component in the solution phase is expected to predominantly solidify as the particle core while the slower component solidifies predominantly as the shell at the end of the drying process. Metaxiotou and Nychas [72] showed experimentally that the binary diffusion coefficient in aqueous PVP solution at 25°C is in the range of 1×10^{-11} m^2 s^{-1} at low concentrations, a value one to two order(s) of magnitude smaller than that of mannitol in water at 4.5% w/w, $\approx 2{\times}10^{-9}$ m^2 s^{-1} computed using Stokes-Einstein, Equation 3. Although the slower diffusivity of PVP may suggest the preferential accumulation of PVP at the surface, it is far more complicated due to the dynamics of the combined system during drying. Particularly, the viscosity of the droplet may increase considerably as the droplet becomes more concentrated. Since $D \propto \frac{1}{\eta}$, this may significantly reduce the diffusivity of mannitol and lead to the formation of a shell containing similar proportion of both components.

Figure 15 supports the above hypothesis as the amount of crystallinity within the particle is observed to decrease (visually) with increase in concentration. This is further confirmed by Raman analysis shown in Figure 13b. The polymorphic outcome from this is discussed below. The decrease in crystallinity also brings about the decrease in particle porosity with increasing PVP concentration, as shown in Figure 12. Similar to the mannitol particles, the observed trend between the porosity obtained from the camera and XCT is followed. From the SEM images and 3D volume rendering from XCT, it is clear that the morphology and microstructure of particles are influenced by the nature of the formulation.

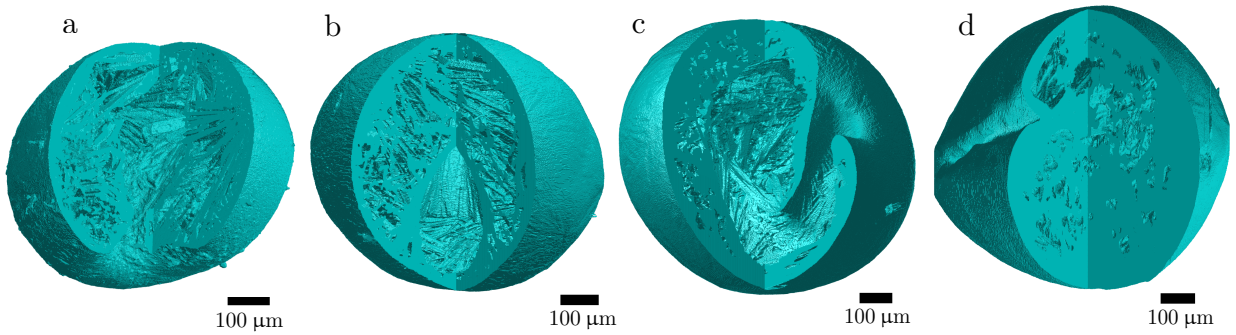

Figure 15: The 3D cross section of the particles obtained from solution droplets containing varying ratios of PVP and mannitol. a) P1-60 b) P3-60 c) P5-60 d) P8-60.

The effect of concentration on the size, porosity and shell thickness of the particle for the range of conditions investigated is summarised in Table 2 and Table 3. Both porosity and particle size increases with concentration in the case of mannitol as expected. When PVP is added, the porosity is seen to decrease with increasing concentration, while the particle size increases to a maximum and then decreases afterwards. On the other hand, the shell thickness increases with increase in PVP concentration (a consequence of the binding property of the polymer), for all the shell thickness metrics described in Section 3.3.4. The increasing shell thickness can also be clearly observed from the XCT images shown in Figure 15.

Table 3: Experimental results for the drying of droplets containing varying starting concentration of PVP in a PVP-mannitol-water formulation [a].

Description	P1-60	P3-60	P5-60	P8-60
Evaporation constant k [10^{-9} m^2 s^{-1}]	4.92±0.3	5.18±0.1	5.01±0.1	5.00±0.1
Final particle size [μm]	590.0 ±18.3	639.8 ±16.7	702.0 ±2	652.2±17.4
Final particle porosity [-]	0.47 ±0.02	0.41 ±0.02	0.33 ±0.02	0.13 ±0.03
Sphericity [-]	0.94 ±0.03	0.93 ±0.04	0.95 ±0.02	0.77 ±0.14
Shell thickness with $\varepsilon > 0.7$ [μm]	15.5 ±1.6	21.9 ±0.3	29.2 ±3.9	- [b]
Shell thickness with $\varepsilon > 0.5$ [μm]	34.5 ±3.0	39.4 ±3.8	56.9 ±7.8	- [b]
Shell thickness with $C_{sf} > 0.5$ [μm]	28.2 ±1.2	29.5 ±1.4	34.3 ±3.5	49.3 ±1.2
Shell thickness with $C_{sf} > 0.3$ [μm]	50.1 ±3.4	52.7 ±4.5	59.5 ±7.8	81.5 ±3.2

[a] A gas flow rate of 1 L min^{-1} is used (determined from parameter fitting see Abdullahi et al. [43]) and a gas relative saturation of 0% in all investigations.

[b] At high concentration of PVP (for example, P8-60), the particles become shrivelled that the resulting solid fraction is low across the particle. Therefore, a shell does not exist explicitly as seen in Figure 15d.

Whereas the α and β polymrophs were obtained from aqueous D-mannitol solutions, the least stable δ polymorph of D-mannitol was manufactured consistently for concentrations up to 7.8% w/w PVP (P8-60) in the presence of PVP, Figure 13b. At concentrations above this (P15-60 and P20-60), the characteristic peaks of the crystalline D-mannitol polymorphs were not observed any more and the amorphous PVP spectrum becomes apparent, indicating the dominating effect of the polymer at these concentrations. The polymorphic outcome of this work agrees well with that obtained from a lab scale spray dryer investigation by Vanhoorne et al. [73], where the δ polymorph was manufactured in the presence of PVP (from 1:4 PVP-mannitol solutions). This starting concentration is approximately that of the P1-60 sample in this work.

4.4. Effect of temperature on particle structure

The effect of drying temperature on particle morphology and microstructure was also investigated. For the range of temperatures considered (i.e., 40 - 80 °C), the particle size in the case of aqueous mannitol solutions remained similar as reported in Table 4. Perhaps, a result of the limited range of conditions investigated. The surface roughness was however observed to decrease with increasing temperature as

599 expected (Figure 16), since the faster evaporation leads to a higher concentration at the droplet surface
600 and hence a higher propensity for nucleation. Lower temperatures favour crystal growth rather than
601 nucleation. This leads to increased particle roughness and the formation of protuberances and results
in lower particle sphericity as shown in Figure 17.

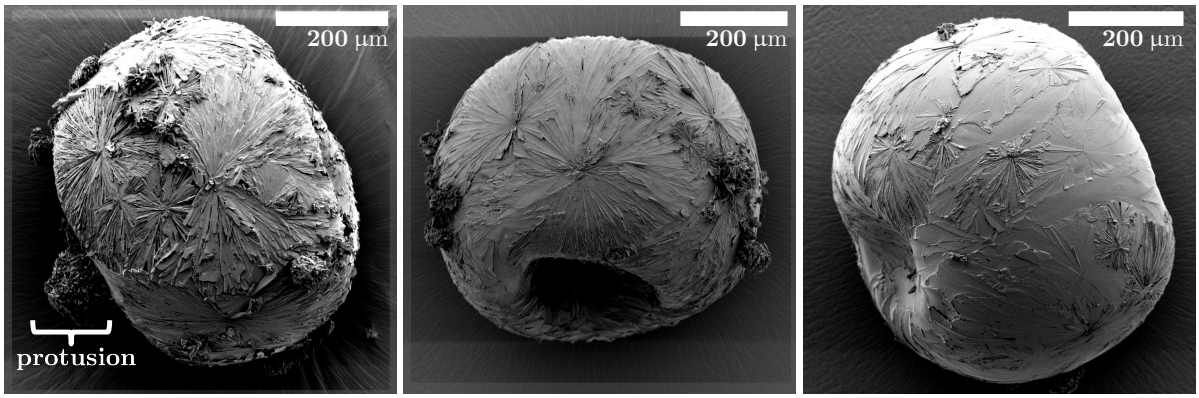

Figure 16: Effect of temperature on a 4.5% w/w mannitol solution, from left to right M5-40, M5-60, M5-80 respectively

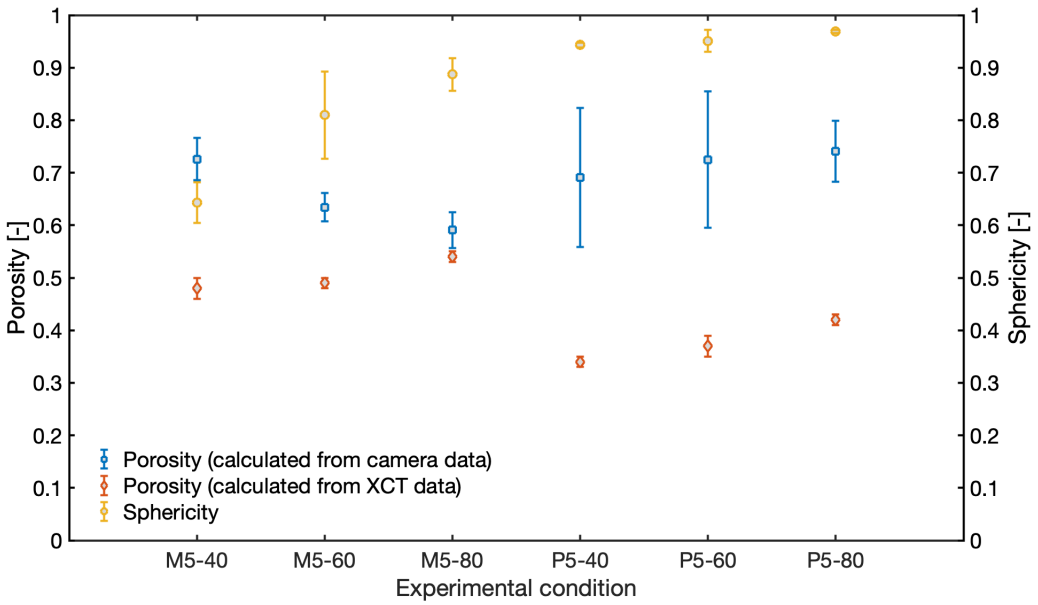

Figure 17: Effect of drying condition on the porosity and sphericity of particles.

602

603 The above results are in qualitative agreement with experimental data reported on lab scale spray dry-
604 ers. Investigations by Maas et al. [74] and Littringer et al. [75] led to the conclusion that the particle
605 size did not change when temperature was varied. However in this work also, the range of temperature

investigated was limited. When a larger range of temperature was considered as in the pilot scale investigation reported by Littringer et al. [75], the particle size was observed to increase with increasing temperature, at least until the particles began to deform considerably at high temperatures. The same authors further demonstrated that increasing the drying temperature led to rougher particles in the lab scale dryer [74–76]. This is indeed surprising from a theoretical point of view since higher drying temperatures should result in more nucleation of crystals and smaller sized crystals overall when compared to slow crystallisation. The authors rationalised this as an effect of delayed crystallisation resulting from the high solution viscosity at the droplet surface. This subsequently led to reduced nucleation at the temperatures investigated. Littringer et al. [75, 77] also showed results for the effect of temperature conducted on a pilot scale dryer. In this case, the results obtained were comparable to the ones observed in the present work with increasing temperature leading to smoother particles.

The larger droplet sizes employed in the acoustic levitation approach and on a pilot scale dryer when compared to the lab scale dryer may be the reason why the particle surface roughness increases with temperature. The time scale of evaporation in the lab scale dryer is between 1 and 2 orders of magnitude smaller (due to the much lower surface area to volume ratio of the droplets) and may indeed result in a highly viscous solution at the droplet surface in the case of a lab scale dryer [78]. The above statement is substantiated by the simulation result shown in Figure 18 (generated with the model reported in Abdullahi et al. [43]). This result demonstrates the effect of process scale on the concentration of mannitol reached at the surface of the droplet. For smaller sized droplets (40 µm) as found in a lab scale operation, the shrinkage is an order of magnitude faster, compared to a size of 140 µm, which is typical in a pilot scale operation. This is also a few orders of magnitude faster than that of a droplet size of 1400 µm typical of single droplet drying [8]. Quantitative evaluation of the particle shell thickness shows that this is similar for the range of temperatures investigated, for all the evaluation criteria defined.

This behaviour is not surprising, particularly if the crystallisation process is the rate limiting step in particle formation. The increase in temperature causes an increase in the solubility of mannitol and an increase in the time to reach saturation at the surface. Although this is in competition with the higher

[8] The simulation proceeds up to a mass fraction of 0.14 (w/w) representing the saturation concentration of the D-mannitol (for the stable β polymorph) in water at the wet bulb temperature of 293 K

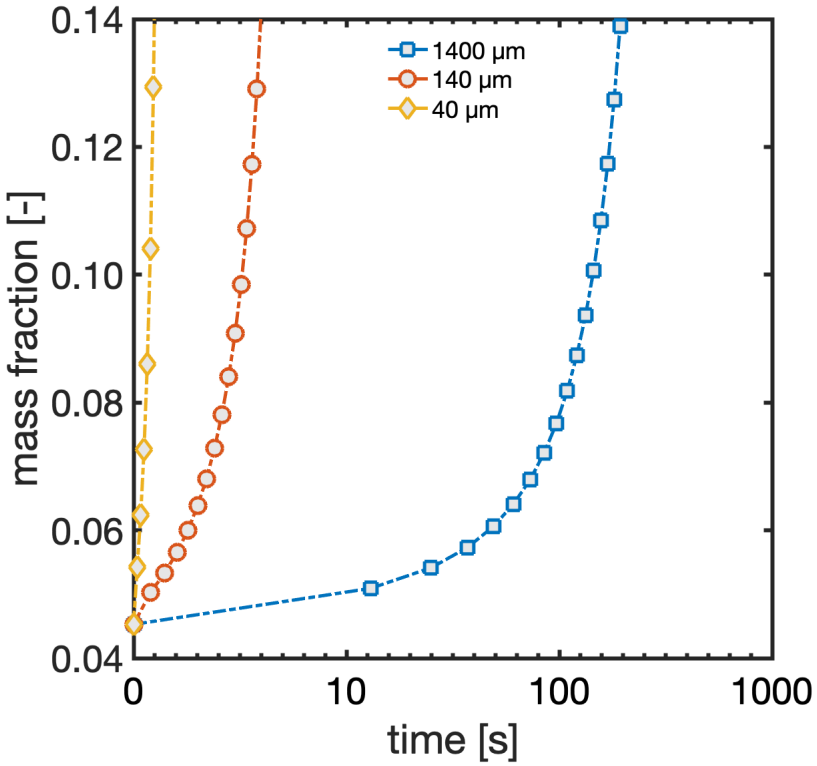

Figure 18: Simulated mass fraction of mannitol (in 4.5% w/w aqueous solution) at the surface during evaporation in a N_2 environment at 60 °C, 0% relative saturation and a gas flow rate of 1 L min^{-1}.

crystallisation kinetics at higher temperatures and the faster drying kinetics, the significant change in the solubility with temperature in the case of mannitol may outweigh the kinetic effects in this case.

The effect of temperature in the presence of PVP was further investigated. The resulting morphologies are illustrated Figure 19. Qualitatively, the particles remain near spherical at the different temperatures. This is confirmed from the sphericity measurement shown in Figure 17. Analysis of the shell thickness shows that an increase in temperature may leads to a decrease in the shell thickness. However, the accuracy of the data in this case suggests a larger variation of temperature needs to be investigated. The effect of temperature on the particle properties is summarised in Table 4.

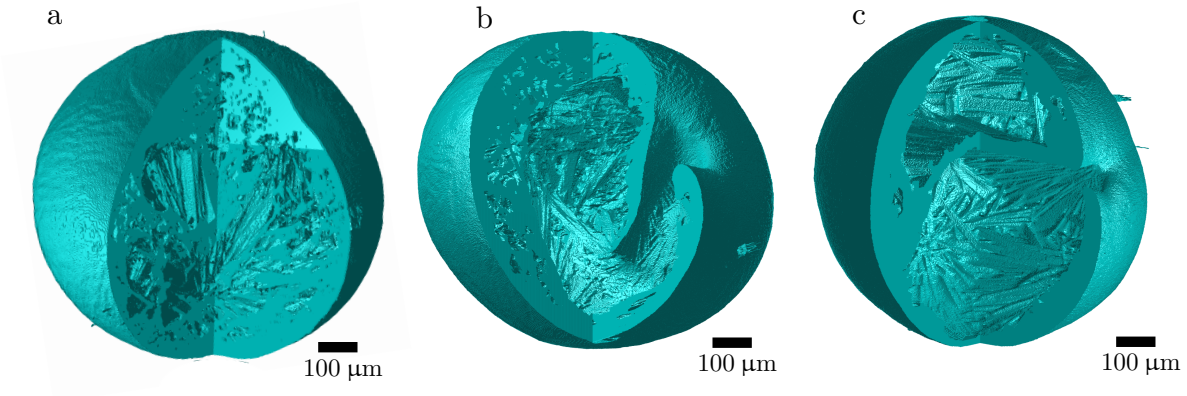

Figure 19: 3D rendered volume of particles obtained at different temperatures from an aqueous solution droplet containing 4.8% w/w PVP and 4.5% w/w mannitol, a) P5-40 b) P5-60 c) P5-80.

Table 4: Experimental results for the drying of mannitol and PVP-mannitol solutions at different temperatures [a].

Description	M5-40	M5-60	M5-80	P5-40	P5-60	P5-80
Evaporation constant k [10^{-9} m^2 s^{-1}]	3.90±0.3	5.18±0.1	6.23±0.3	3.30±0.1	5.18±0.1	6.72±0.3
Peclet number Pe [-]	0.75	0.94	0.94	-[b]	-[b]	-[b]
Final particle size [µm]	517±2.3	552.8±5.5	539.5±3.1	683.8±5.5	702.0±2	752±3.7
Final particle porosity [-]	0.48±0.02	0.49±0.01	0.54±0.01	0.34±0.01	0.37±0.02	0.42±0.01
Sphericity [-]	0.64 ±0.04	0.81 ±0.08	0.89 ±0.03	0.94 ±0.01	0.95 ±0.02	0.97 ±0.01
Shell thickness with $\varepsilon > 0.3$ [µm]	8.2±1.0	6.5±1.0	12.4±1.0	40.6±1.0	29.2±4	27.0±2
Shell thickness with $\varepsilon > 0.5$) [µm]	27.5±13.0	21.1±6.4	25.5±2.0	68.4±4.0	56.9±8.0	64.0±9.0
Shell thickness with $C_{sf} > 0.5$ [µm]	41.1 ±3.9	34.0 ±2.0	29.7 ±1.0	36.9 ±2.8	34.3 ±3.5	39.3 ±2.6
Shell thickness with $C_{sf} > 0.3$ [µm]	76.0 ±1.6	59.7 ±2.3	54.7 ±2.1	61.4 ±2.8	59.5 ±7.8	63.6 ±2.0

[a] A gas flow rate of 1 L min^{-1}, a gas relative saturation of 0% in all investigations.

[b] Equation 1 was used to calculate the Peclet number in the binary systems. However this does not directly apply to a ternary system. Therefore we have not attempted to calculate this but rather, we have used the information of the binary diffusion coefficient of each component in the solvent to understand the behaviour of the particles as discussed in the main text above.

5. Conclusions

X-ray computed tomography (XCT) was used to elucidate the morphology and microstructure of particles obtained from drying solution droplets containing mannitol or mannitol and PVP in water. The implementation of an expansive image analysis algorithm for the XCT images was important in order to extract essential architectural features of the particles. Surface and microstructure information was extracted using a combination of the image analysis algorithm employed and scanning electron microscopy (SEM). Data obtained from camera images were used to quantify the porosity of the particles

and were compared to that obtained from XCT. By considering the effect of formulation properties and drying conditions, one can determine how particles of a desired characteristic (i.e., size, sphericity, porosity, surface roughness etc.) can be manufactured for a specific application.

The effect of mannitol concentration in aqueous solution demonstrated the opportunity to manufacture particles with different level of crystallinity. The particle size and surface roughness was observed to increase with increasing mannitol concentration, although the difference in shell thickness was not conclusive. Characterisation of the particles using Raman spectroscopy showed the ability to manufacture the metastable α polymorph at low concentration (up to $\approx 7\%$). The more stable β form appeared at a higher concentration, which was probably due to the stochastic nature of the concomitant crystallisation of mannitol [70, 71].

On the addition of a polymeric binder (PVP), the particle morphologies remained similar with blow holes. However, the particles became significantly smoother, owing to the non-crystalline skin forming nature of the polymer and the inhibition of nucleation and growth of crystals of mannitol. The particle size was observed to increase with increasing PVP concentration until it reaches a turning point, where the shell completely collapses leading to complete particle deformation. The manufactured particles therefore exhibits a significantly lower porosity and overall volume. At the same time, the shell thickness increases due to the binding property of the polymer and the polymorphic form changes to the least stable δ form.

The effect of temperature (40 °C - 80 °C) was also investigated. In the case of aqueous mannitol solution, the particle size and shell thickness remained similar for the range of temperature considered. However, the surface roughness of the particle was observed to decrease with increasing temperature. A result of the faster crystallisation at higher temperatures. Generally, the sphericity of the particles (describing its shape) decreases with increase in the formation of protuberances. Comparison between porosity values obtained from the camera and XCT were unmatched, but similar trends were observed. The result obtained was compared to that from a lab and pilot scale operation [64, 65, 76] and shows good similarity.

In both the single droplet drying experiment employed here and the spray drying experiments, rigid porous particles were obtained. Although at lab scale, increasing temperature was shown to lead to

rougher particles. The difference in results of the lab scale from that obtained using the acoustic levitation and for drying at pilot scale was rationalised to be the effect of droplet size on the mechanism of crystallisation. In the case of PVP, similar morphologies were also observed, although the particle sizes were observed to increase for the same range of conditions. Such a detailed analysis of particle morphology development and microstructure can be used to inform product and process development. Additionally, the result obtained here may be useful for researchers aiming to develop predictive droplet drying models that incorporate microstructure information. We believe that such models could form the basis for further advancements in the in-depth description of spray drying operations.

Acknowledgements

This work was supported by the Eli Lilly Research Award Program (LRAP). The authors would like to acknowledge the Engineering and Physical Science Research Council (EPSRC) for funding the Henry Moseley X-ray Imaging Facility (HMXIF), which has been made available through the Royce Institute for Advanced Materials through grants (EP/F007906/1, EP/F001452/1, EP/I02249X, EP/M010619/1, EP/F028431/1, EP/M022498/1 and EP/R00661X/1). The authors are also grateful to Julia Behnsen at the HMXIF for the useful discussions surrounding the research and for providing the required trainings.

References

[1] S. Mangal, F. Meiser, D. Morton, I. Larson, Particle Engineering of Excipients for Direct Compression: Understanding the Role of Material Properties, Current Pharmaceutical Design 21 (40) (2015) 5877–5889, ISSN 13816128, doi:10.2174/1381612821666151008125117.

[2] K. M. Carver, R. C. Snyder, Unexpected polymorphism and unique particle morphologies from monodisperse droplet evaporation, Industrial and Engineering Chemistry Research 51 (48) (2012) 15720–15728, ISSN 08885885, doi:10.1021/ie3015439.

[3] R. A. Halliwell, R. M. Bhardwaj, C. J. Brown, N. E. Briggs, J. Dunn, J. Robertson, A. Nordon, A. J. Florence, Spray Drying as a Reliable Route to Produce Metastable Carbamazepine Form IV, Journal of Pharmaceutical Sciences 106 (7) (2017) 1874–1880, ISSN 15206017, doi:10.1016/j.xphs.2017.03.045.

[4] F. Lyu, J. J. Liu, Y. Zhang, X. Z. Wang, Combined control of morphology and polymorph in spray drying of mannitol for dry powder inhalation, Journal of Crystal Growth 467 (2017) 155–161, ISSN 00220248, doi:10.1016/j.jcrysgro.2017.03.033.

[5] J. F. Bauer, Pharmaceutical Solids The Amorphous Phase, Journal of Validation Technology 15 (3 (Summer)) (2009) 63–68.

[6] M. I. Ré, Formulating drug delivery systems by spray drying, doi:10.1080/07373930600611877, 2006.

[7] P. Thybo, L. Hovgaard, J. S. Lindeløv, A. Brask, S. K. Andersen, Scaling up the spray drying process from pilot to production scale using an atomized droplet size criterion, Pharmaceutical Research 25 (7) (2008) 1610–1620, ISSN 07248741, doi:10.1007/s11095-008-9565-8.

[8] D. E. Walton, C. J. Mumford, Spray dried products-characterization of particle morphology, Chemical Engineering Research and Design 77 (1) (1999) 21–38, ISSN 02638762, doi:10.1205/026387699525846.

[9] D. E. Walton, C. J. Mumford, The morphology of spray-dried particles. The effect of process variables upon the morphology of spray-dried particles, Chemical Engineering Research and Design 77 (5) (1999) 442–460, ISSN 02638762, doi:10.1205/026387699526296.

[10] D. E. Walton, The morphology of spray-dried particles a qualitative view, Drying Technology 18 (9) (2000) 1943–1986, ISSN 07373937, doi:10.1080/07373930008917822.

[11] M. Mönckedieck, J. Kamplade, P. Fakner, N. A. Urbanetz, P. Walzel, H. Steckel, R. Scherließ, Spray drying of mannitol carrier particles with defined morphology and flow characteristics for dry powder inhalation, Drying Technology 35 (15) (2017) 1843–1857, ISSN 15322300, doi:10.1080/07373937.2017.1281291.

[12] J. Rantanen, J. Khinast, The Future of Pharmaceutical Manufacturing Sciences., Journal of pharmaceutical sciences 104 (11) (2015) 3612–38, ISSN 1520-6017, doi:10.1002/jps.24594.

[13] Y. Huang, W.-G. Dai, Fundamental aspects of solid dispersion technology for poorly soluble drugs, Acta Pharmaceutica Sinica B 4 (1) (2013) 18–25, ISSN 22113835, doi:10.1016/j.apsb.2013.11.001.

[14] S. V. Jermain, C. Brough, R. O. Williams, Amorphous solid dispersions and nanocrystal technologies for poorly water-soluble drug delivery An update, International Journal of Pharmaceutics 535 (1-2) (2018) 379–392, ISSN 18733476, doi:10.1016/j.ijpharm.2017.10.051.

[15] E. Johansen Crosby, Spray Drying Handbook, Drying Technology 7 (2) (1989) 419–425, ISSN 0737-3937, doi:10.1080/07373938908916598.

[16] E. M. Both, M. Nuzzo, A. Millqvist-Fureby, R. M. Boom, M. A. Schutyser, Morphology development during single droplet drying of mixed component formulations and milk, Food Research International 109 (2018) 448–454, ISSN 18737145, doi:10.1016/j.foodres.2018.04.043.

[17] F. J. Doerr, I. D. Oswald, A. J. Florence, Quantitative investigation of particle formation of a model pharmaceutical formulation using single droplet evaporation experiments and X-ray tomography, Advanced Powder Technology 29 (12) (2018) 2996–3006, ISSN 15685527, doi:10.1016/j.apt.2018.09.027.

[18] K. H. Leong, Morphological control of particles generated from the evaporation of solution droplets: Experiment, Journal of Aerosol Science 18 (5) (1987) 525–552, ISSN 00218502, doi:10.1016/0021-8502(87)90067-X.

744 [19] N. Tsapis, E. R. Dufresne, S. S. Sinha, C. S. Riera, J. W. Hutchinson, L. Mahadevan, D. A. Weitz,
745 Onset of buckling in drying droplets of colloidal suspensions, Physical Review Letters 94 (1),
746 ISSN 00319007, doi:10.1103/PhysRevLett.94.018302.

747 [20] M. Nuzzo, J. Sloth, B. Bergenstahl, A. Millqvist-Fureby, Phase Segregation in Individually Dried
748 Particles Composed of Biopolymers, Langmuir 31 (40) (2015) 10946–10954, ISSN 15205827,
749 doi:10.1021/acs.langmuir.5b02023.

750 [21] M. Nuzzo, J. Sloth, B. Brandner, B. Bergenstahl, A. Millqvist-Fureby, Confocal Raman mi-
751 croscopy for mapping phase segregation in individually dried particles composed of lactose and
752 macromolecules, Colloids and Surfaces A: Physicochemical and Engineering Aspects 481 (2015)
753 229–236, ISSN 18734359, doi:10.1016/j.colsurfa.2015.04.044.

754 [22] M. Munoz-Ibanez, M. Nuzzo, C. Turchiuli, B. Bergenståhl, E. Dumoulin, A. Millqvist-Fureby,
755 The microstructure and component distribution in spray-dried emulsion particles, Food Structure
756 8 (2016) 16–24, ISSN 22133291, doi:10.1016/j.foostr.2016.05.001.

757 [23] B. Crean, A. Parker, D. L. Roux, M. Perkins, S. Y. Luk, S. R. Banks, C. D. Melia, C. J. Roberts,
758 Elucidation of the internal physical and chemical microstructure of pharmaceutical granules us-
759 ing X-ray micro-computed tomography, Raman microscopy and infrared spectroscopy, European
760 Journal of Pharmaceutics and Biopharmaceutics 76 (3) (2010) 498–506, ISSN 09396411, doi:
761 10.1016/j.ejpb.2010.08.006.

762 [24] F. J. Doerr, A. J. Florence, A micro-XRT image analysis and machine learning methodology for
763 the characterisation of multi-particulate capsule formulations, International Journal of Pharma-
764 ceutics: X 2, ISSN 25901567, doi:10.1016/j.ijpx.2020.100041.

765 [25] E. N. Landis, D. T. Keane, X-ray microtomography, Materials Characterization 61 (12) (2010)
766 1305–1316, ISSN 10445803, doi:10.1016/j.matchar.2010.09.012.

767 [26] A. Farshchi, A. Hassanpour, A. E. Bayly, The structure of spray-dried detergent powders, Powder
768 Technology 355 (2019) 738–754, ISSN 1873328X, doi:10.1016/j.powtec.2019.06.049.

769 [27] A. Farshchi, A. Hassanpour, R. Ettelaie, A. E. Bayly, Evolution of surface micro-structure and

770 moisture sorption characteristics of spray-dried detergent powders, Journal of Colloid and Inter-
771 face Science 551 (2019) 283–296, ISSN 10957103, doi:10.1016/j.jcis.2019.04.069.

772 [28] R. Kajihara, S. Noguchi, Y. Iwao, Y. Yasuda, M. Segawa, S. Itai, Structural investigation of spheri-
773 cal hollow excipient Mannit Q by X-ray microtomography, International Journal of Pharmaceutics
774 495 (1) (2015) 140–143, ISSN 18733476, doi:10.1016/j.ijpharm.2015.08.097.

775 [29] J. Bouman, P. Venema, R. J. de Vries, E. van der Linden, M. A. Schutyser, Hole and vacuole
776 formation during drying of sessile whey protein droplets, Food Research International 84 (2016)
777 128–135, ISSN 09639969, doi:10.1016/j.foodres.2016.03.027.

778 [30] L. Farber, G. Tardos, J. N. Michaels, Use of X-ray tomography to study the porosity and
779 morphology of granules, Powder Technology 132 (1) (2003) 57–63, ISSN 00325910, doi:
780 10.1016/S0032-5910(03)00043-3.

781 [31] G. Perfetti, E. V. D. Casteele, B. Rieger, W. J. Wildeboer, G. M. Meesters, X-ray micro tomogra-
782 phy and image analysis as complementary methods for morphological characterization and coat-
783 ing thickness measurement of coated particles, Advanced Powder Technology 21 (6) (2010) 663–
784 675, ISSN 09218831, doi:10.1016/j.apt.2010.08.002.

785 [32] L. Fang, X. Yin, L. Wu, Y. He, Y. He, W. Qin, F. Meng, P. York, X. Xu, J. Zhang, Classification
786 of microcrystalline celluloses via structures of individual particles measured by synchrotron radi-
787 ation X-ray micro-computed tomography, International Journal of Pharmaceutics 531 (2) (2017)
788 658–667, ISSN 18733476, doi:10.1016/j.ijpharm.2017.05.019.

789 [33] F. Sondej, A. Bück, K. Koslowsky, P. Bachmann, M. Jacob, E. Tsotsas, Investigation of coating
790 layer morphology by micro-computed X-ray tomography, Powder Technology 273 (2015) 165–
791 175, ISSN 1873328X, doi:10.1016/j.powtec.2014.12.050.

792 [34] A. P. Dhawan, Medical Image Analysis, John Wiley & Sons, Inc, New Jersey, second edn., ISBN
793 9780470622056, doi:10.1002/9780470918548, 2011.

794 [35] N. Fu, M. W. Woo, X. D. Chen, Single Droplet Drying Technique to Study Drying Kinetics
795 Measurement and Particle Functionality: A Review, Drying Technology 30 (15) (2012) 1771–
796 1785, ISSN 07373937, doi:10.1080/07373937.2012.708002.

[36] M. Nuzzo, A. Millqvist-Fureby, J. Sloth, B. Bergenstahl, Surface Composition and Morphology of Particles Dried Individually and by Spray Drying, Drying Technology 33 (6) (2015) 757–767, ISSN 15322300, doi:10.1080/07373937.2014.990566.

[37] E. M. Both, R. M. Boom, M. A. Schutyser, Particle morphology and powder properties during spray drying of maltodextrin and whey protein mixtures, Powder Technology 363 (2020) 519–524, ISSN 1873328X, doi:10.1016/j.powtec.2020.01.001.

[38] I. Gouaou, S. Shamaei, M. S. Koutchoukali, M. Bouhelassa, E. Tsotsas, A. Kharaghani, Impact of operating conditions on a single droplet and spray drying of hydroxypropylated pea starch: Process performance and final powder properties, Asia-Pacific Journal of Chemical Engineering 14 (1), ISSN 19322143, doi:10.1002/apj.2268.

[39] N. Fu, M. W. Woo, X. D. Chen, Single Droplet Drying Technique to Study Drying Kinetics Measurement and Particle Functionality: A Review, Drying Technology 30 (15) (2012) 1771–1785, ISSN 07373937, doi:10.1080/07373937.2012.708002.

[40] F. K. Gregson, J. F. Robinson, R. E. Miles, C. P. Royall, J. P. Reid, Drying Kinetics of Salt Solution Droplets: Water Evaporation Rates and Crystallization, Journal of Physical Chemistry B 123 (1) (2019) 266–276, ISSN 15205207, doi:10.1021/acs.jpcb.8b09584.

[41] X. D. Chen, H. Sidhu, M. Nelson, Theoretical probing of the phenomenon of the formation of the outermost surface layer of a multi-component particle, and the surface chemical composition after the rapid removal of water in spray drying, Chemical Engineering Science 66 (24) (2011) 6375–6384, ISSN 00092509, doi:10.1016/j.ces.2011.08.035.

[42] M. Nuzzo, J. Sloth Overgaard, B. Bergenståhl, A. Millqvist-Fureby, The morphology and internal composition of dried particles from whole milkFrom single droplet to full scale drying, Food Structure 13 (2017) 35–44, ISSN 22133291, doi:10.1016/j.foostr.2017.02.001.

[43] H. Abdullahi, C. L. Burcham, T. Vetter, A mechanistic model to predict droplet drying history and particle shell formation in multicomponent systems, Chemical Engineering Science 224 (2020) 115713, ISSN 00092509, doi:10.1016/j.ces.2020.115713.

[44] C. S. Handscomb, M. Kraft, A. E. Bayly, A new model for the drying of droplets containing suspended solids, Chemical Engineering Science 64 (4) (2009) 628–637, ISSN 00092509, doi:10.1016/j.ces.2008.04.051.

[45] C. Handscomb, M. Kraft, A. Bayly, A new model for the drying of droplets containing suspended solids after shell formation, Chemical Engineering Science 64 (2) (2009) 228–246, ISSN 00092509, doi:10.1016/j.ces.2008.10.019.

[46] P. Seydel, A. Sengespeick, J. Blömer, J. Bertling, Experiment and mathematical modeling of solid formation at spray drying, Chemical Engineering and Technology 27 (5) (2004) 505–510, ISSN 09307516, doi:10.1002/ceat.200403218.

[47] E. Boel, R. Koekoekx, S. Dedroog, I. Babkin, M. R. Vetrano, C. Clasen, G. Van den Mooter, Unraveling particle formation: From single droplet drying to spray drying and electrospraying, Pharmaceutics 12 (7) (2020) 1–58, ISSN 19994923, doi:10.3390/pharmaceutics12070625.

[48] S. Nešić, J. Vodnik, Kinetics of droplet evaporation, Chemical Engineering Science 46 (2) (1991) 527–537, ISSN 00092509, doi:10.1016/0009-2509(91)80013-O.

[49] L. Alamilla-Beltrán, J. J. Chanona-Pérez, A. R. Jiménez-Aparicio, G. F. Gutiérrez-Lopez, Description of morphological changes of particles along spray drying, Journal of Food Engineering 67 (1-2) (2005) 179–184, ISSN 02608774, doi:10.1016/j.jfoodeng.2004.05.063.

[50] R. Vehring, W. R. Foss, D. Lechuga-Ballesteros, Particle formation in spray drying, Journal of Aerosol Science 38 (7) (2007) 728–746, ISSN 00218502, doi:10.1016/j.jaerosci.2007.04.005.

[51] B. Abramzon, W. A. Sirignano, Droplet vaporization model for spray combustion calculations, International Journal of Heat and Mass Transfer 32 (9) (1989) 1605–1618, ISSN 00179310, doi:10.1016/0017-9310(89)90043-4.

[52] S. K. Aggarwal, A. Y. Tong, W. A. Sirignano, A comparison of vaporization models in spray calculations, AIAA Journal 22 (10) (1984) 1448–1457, ISSN 00011452, doi:10.2514/3.8802.

[53] E. B. Poling, M. J. Prausnitz, P. O'Connell, The properties of Liquids and Gases, McGraw Hill, Chicago, 5th edn., ISBN 0071499997, doi:10.1036/0070116822, 2001.

[54] C. Groenewold, C. Möser, H. Groenewold, E. Tsotsas, Determination of single-particle drying kinetics in an acoustic levitator, Chemical Engineering Journal 86 (1-2) (2002) 217–222, ISSN 13858947, doi:10.1016/S1385-8947(01)00292-3.

[55] O. Kastner, G. Brenn, D. Rensink, C. Tropea, The acoustic tube levitator - A novel device for determining the drying kinetics of single droplets, Chemical Engineering and Technology 24 (4) (2001) 335–339, ISSN 09307516, doi:10.1002/1521-4125(200104)24:4⟨335::AID-CEAT335⟩3.0.CO;2-8.

[56] N. Otsu, Threshold Selection Method From Gray-Level Histograms., IEEE Trans Syst Man Cybern SMC-9 (1) (1979) 62–66, ISSN 00189472, doi:10.1109/TSMC.1979.4310076.

[57] W. E. Ranz, W. R. Marshall, Evaporation from drops. Parts I & II., Chem. Eng. Progr 48 (22) (1952) 141–173, ISSN 09247963, doi:10.1016/S0924-7963(01)00032-X.

[58] A. L. Yarin, G. Brenn, O. Kastner, D. Rensink, C. Tropea, Evaporation of acoustically levitated droplets, Journal of Fluid Mechanics 399 (1999) 151–204, ISSN 00221120, doi:10.1017/S0022112099006266.

[59] A. L. Yarin, G. Brenn, J. Keller, M. Pfaffenlehner, E. Ryssel, C. Tropea, Flowfield characteristics of an aerodynamic acoustic levitator, Physics of Fluids 9 (11) (1997) 3300–3314, ISSN 10706631, doi:10.1063/1.869444.

[60] E. H. Trinh, J. L. Robey, Experimental study of streaming flows associated with ultrasonic levitators, Physics of Fluids 6 (11) (1994) 3567–3579, ISSN 10706631, doi:10.1063/1.868415.

[61] R. Tuckermann, S. Bauerecker, B. Neidhart, Evaporation rates of alkanes and alkanols from acoustically levitated drops, Analytical and Bioanalytical Chemistry 372 (1) (2002) 122–127, ISSN 16182642, doi:10.1007/s00216-001-1132-7.

[62] G. Perini, F. Salvatori, D. R. Ochsenbein, M. Mazzotti, T. Vetter, Filterability prediction of needle-like crystals based on particle size and shape distribution data, Separation and Purification Technology 211 (2019) 768–781, ISSN 18733794, doi:10.1016/j.seppur.2018.10.042.

874 [63] B. Pathak, S. Basu, Modulation of Buckling Dynamics in Nanoparticle Laden Droplets Using Ex-
875 ternal Heating, Langmuir 32 (11) (2016) 2591–2600, ISSN 15205827, doi:10.1021/acs.langmuir.
876 6b00544.

877 [64] S. G. Maas, G. Schaldach, E. M. Littringer, A. Mescher, U. J. Griesser, D. E. Braun, P. E. Walzel,
878 N. A. Urbanetz, The impact of spray drying outlet temperature on the particle morphology of man-
879 nitol, Powder Technology 213 (1) (2011) 27–35, ISSN 00325910, doi:10.1016/j.powtec.2011.06.
880 024.

881 [65] E. Lintingre, F. Lequeux, L. Talini, N. Tsapis, Control of particle morphology in the spray drying
882 of colloidal suspensions, Soft Matter 12 (36) (2016) 7435–7444, ISSN 17446848, doi:10.1039/
883 c6sm01314g.

884 [66] T. T. Tran, J. G. Avila-Acevedo, E. Tsotsas, Enhanced methods for experimental investigation of
885 single droplet drying kinetics and application to lactose/water, Drying Technology 34 (10) (2016)
886 1185–1195, ISSN 15322300, doi:10.1080/07373937.2015.1100202.

887 [67] F. R. Fronczek, H. N. Kamel, M. Slattery, Three polymorphs (α, β, and δ) of d-mannitol at 100 K,
888 Acta Crystallographica Section C: Crystal Structure Communications 59 (10), ISSN 01082701,
889 doi:10.1107/S0108270103018961.

890 [68] J. Cornel, P. Kidambi, M. Mazzotti, Precipitation and transformation of the three polymorphs
891 of d-mannitol, Industrial and Engineering Chemistry Research 49 (12) (2010) 5854–5862, ISSN
892 08885885, doi:10.1021/ie9019616.

893 [69] W. Su, N. Jia, H. Li, H. Hao, C. Li, Polymorphism of D-mannitol: Crystal structure and the
894 crystal growth mechanism, Chinese Journal of Chemical Engineering 25 (3) (2017) 358–362,
895 ISSN 10049541, doi:10.1016/j.cjche.2016.09.002.

896 [70] J. Tao, L. Yu, Kinetics of cross-nucleation between polymorphs, Journal of Physical Chemistry B
897 110 (14) (2006) 7098–7101, ISSN 15206106, doi:10.1021/jp060694j.

898 [71] J. Tao, K. J. Jones, L. Yu, Cross-nucleation between D-mannitol polymorphs in seeded crystal-
899 lization, Crystal Growth and Design 7 (12) (2007) 2410–2414, ISSN 15287483, doi:10.1021/
900 cg070387i.

[72] Z. A. Metaxiotou, S. G. Nychas, Experimental measurement of diffusion in aqueous polyvinylpyrrolidone solutions, AIChE Journal 41 (4) (1995) 812–818, ISSN 15475905, doi:10.1002/aic.690410408.

[73] V. Vanhoorne, P. J. Van Bockstal, B. Van Snick, E. Peeters, T. Monteyne, P. Gomes, T. De Beer, J. P. Remon, C. Vervaet, Continuous manufacturing of delta mannitol by cospray drying with PVP, International Journal of Pharmaceutics 501 (1-2) (2016) 139–147, ISSN 18733476, doi:10.1016/j.ijpharm.2016.02.001.

[74] S. G. Maas, G. Schaldach, P. E. Walzel, N. A. Urbanetz, Tailoring dry powder inhaler performance by modifying carrier surface topography by spray drying, Atomization and Sprays 20 (9) (2010) 763–774, ISSN 10445110, doi:10.1615/AtomizSpr.v20.i9.20.

[75] E. M. Littringer, R. Paus, A. Mescher, H. Schroettner, P. Walzel, N. A. Urbanetz, The morphology of spray dried mannitol particles - The vital importance of droplet size, Powder Technology 239 (2013) 162–174, ISSN 00325910, doi:10.1016/j.powtec.2013.01.065.

[76] E. M. Littringer, M. F. Noisternig, A. Mescher, H. Schroettner, P. Walzel, U. J. Griesser, N. A. Urbanetz, The morphology and various densities of spray dried mannitol, Powder Technology 246 (2013) 193–200, ISSN 00325910, doi:10.1016/j.powtec.2013.05.004.

[77] E. M. Littringer, A. Mescher, H. Schroettner, L. Achelis, P. Walzel, N. A. Urbanetz, Spray dried mannitol carrier particles with tailored surface properties - The influence of carrier surface roughness and shape, European Journal of Pharmaceutics and Biopharmaceutics 82 (1) (2012) 194–204, ISSN 09396411, doi:10.1016/j.ejpb.2012.05.001.

[78] E. M. Both, I. Siemons, R. M. Boom, M. A. Schutyser, The role of viscosity in morphology development during single droplet drying, Food Hydrocolloids 94 (2019) 510–518, ISSN 0268005X, doi:10.1016/j.foodhyd.2019.03.023.